A Comparison of Solid Electrolyte Interphase Formation and Evolution on Highly Oriented Pyrolytic and Disordered Graphite Negative Electrodes in Lithium-ion Batteries

Haoyu Zhu [a], Joshua Russell [a], Zongtang Fang [b], Pete Barnes [a], Lan Li [a,c], Corey Efaw [a,d], Allison Muenzer [a], Jeremy May [e], Kailash Hamal [e], I. Francis Cheng [e], Paul Davis [a], Eric Dufek [d,], and Hui Xiong [a,c,]**

[a] Micron School of Materials Science and Engineering, Boise State University, Boise, ID 83725, USA

[b] Biological and Chemical Science and Engineering Department, Idaho National Laboratory, Idaho Falls, ID 83415, USA

[c] Center for Advanced Energy Studies, Idaho Falls, ID 83401, USA

[d] Energy Storage & Advanced Transportation Department, Idaho National Laboratory, Idaho Falls, ID 83415, USA

[e] Department of Chemistry, University of Idaho, Moscow, ID 83843, USA

*E-mail: clairexiong@boisestate.edu; eric.dufek@inl.gov (corresponding authors)

KEYWORDS: SEI formation and evolution, graphite electrodes, defect, operando electrochemical AFM, Li-ion batteries

ABSTRACT

The presence and stability of solid electrolyte interphase (SEI) on graphitic electrodes is vital to the long-term performance of lithium ion batteries (LIBs). However, the formation and evolution of SEI remain the least understood area in LIBs due to its dynamic nature, complexity in chemical composition, heterogeneity in morphology, as well as lack of reliable *in situ*/operando techniques for accurate characterization. In addition, chemical composition and morphology of SEI are not only affected by the choice of electrolyte, but also by the nature of the electrode surface. While introduction of defects into graphitic electrodes has promoted their electrochemical properties,

how such structural defects influence SEI formation and evolution remains an open question. Here, utilizing non-destructive operando electrochemical atomic force microscopy (EChem-AFM) we systematically monitor and compare the *dynamic* SEI formation and evolution on a pair of representative graphitic materials with and without defects, namely highly oriented pyrolytic and disordered graphite electrodes. Complement to the characterization of SEI topographical and mechanical changes during electrochemical cycling by EChem-AFM, chemical analysis and theoretical calculations are conducted to provide mechanistic insights underlying SEI formation and evolution. The results provide guidance to engineer functional SEIs through design of carbon materials with defects for LIBs and beyond.

1. Introduction

Since lithium ion batteries (LIBs) were first commercialized by Sony in 1991, they have found wide applications in both electric vehicles and portable electronics due to their high energy and power densities.[1-4] Graphite is the most commonly used negative electrode (anode) material in LIBs due to its low potential for reversible lithium intercalation/deintercalation (~0.1V vs Li^+/Li), relatively high theoretical capacity of 372 mAh/g, and good cycling stability.[5] The electrochemical processes occurring at the electrode/electrolyte interface are crucial to the performance of LIBs. During the initial lithiation of a graphite electrode, the electrolyte solvents and salts may be reduced and decomposed at low potentials. The decomposition products form a thin layer on the graphite surface known as the solid electrolyte interphase (SEI). SEI formation requires the consumption of lithium ions, which leads to an irreversible capacity loss.[5-7] However, once formed, a good SEI acts as a passivating layer that prevents further undesired electrochemical reductions of the electrolyte, hence additional capacity loss and Li ion consumption, due to its ion-conducting but electron-impeding nature. Therefore, the presence and stability of the SEI is essential for cycle life, aging behaviors, as well as rate capability and safety of practical LIBs.[8] As such, understanding SEI composition, formation and evolution is of critical importance to the design and development of high-performance LIBs.

Several models of SEI have been previously introduced, the earliest of which was proposed by Peled.[8, 9] His initial model included a single layer and then it was modified to a bilayer structure consisting of a thin, compact inner layer and a thicker but porous outer layer. Later, a further modified model was proposed: a "mosaic"-type SEI, which may

contain polyhetero microphases of several different components, including inorganic LiF, Li_2O, and Li_2CO_3 close to the electrode surface whereas organic polyolefins and semicarbonates closer to the interface with the electrolyte.[10] Soon after, Aurbach et al. also suggested that SEI has a multilayered, mosaic-type structure.[11] In 2004, a continuum SEI growth model was proposed.[12] In 2006, Edstrom et al. reported conclusive experimental results which suggested that LiF is formed in the SEI while Li_2O, often reported to be present in the SEI, could be an artifact from abusive Ar^+ sputtering and the presence of Li_2CO_3 is a matter of debate.[13-15] In 2014, Cresce et al. observed time evolution of 3D SEI formation on highly oriented pyrolytic graphite (HOPG) through electrochemical atomic force microscopy (EChem-AFM).[16] In 2019, utilizing in situ characterization techniques, Liu et al. reported LiF and lithium alkylcarbonates as the main chemical SEI components for graphite electrode at different potentials.[17] They further confirmed that cyclic carbonate molecules are preferentially reduced over acyclic carbonate molecules, making their reduction product the major SEI component. Later that year, through organic synthesis and rigorous characterizations, Wang et al. determined the main organic SEI component of graphite electrode in ethylene carbonate (EC) based electrolyte is lithium ethylene mono-carbonate (LEMC) instead of lithium ethylene di-carbonate (LEDC), which challenges the previous perception of the prevailing organic SEI component.[18] Until today, SEI is still regarded as "the most important but least understood (component) in lithium ion batteries" possibly due to difficulties during sample preparation, transfer or characterization processes, instability and complexity of SEI, and insufficient direct measurements of its physicochemical properties as stated in recent reviews and reports.[17, 19-26] Hence, fundamental understanding is still needed to unambiguously determine what and how SEI

components are formed, arranged and evolved on graphite surface, and how electrolyte and chemical structure of the electrode surface influence it.

Despite the importance of understanding the formation, chemical composition, arrangement, structural, chemical, mechanical and morphological evolution of the SEI, much remains to be understood at the fundamental level due to measurement difficulties. Due to the reactivity of SEI with moisture and air and the potential structural change during preparation for postmortem analysis, *in situ*/operando methods are preferred for characterization of SEI. A wide variety of *in situ* techniques have been employed in the study of SEI, including X-ray scattering methods, scanning electron microscopy, ellipsometry, transmission electron microscopy, and neutron reflectometry.[27-31] *In situ* atomic force microscopy (AFM) and related scanning probe microscopy methods are among the most widely applied.[16, 22, 31-36] These techniques allow one to directly observe the physical processes of SEI formation and growth on electrode surfaces. Highly oriented pyrolytic graphite (HOPG) is often used as a platform for AFM studies due to its atomically flat and almost defect-free surface. Using *in situ* AFM, it was previously reported that SEI formation on basal-plane HOPG starts at potentials below 0.7 V vs. Li/Li^+ in EC-based electrolyte.[32-35, 37] At the edge plane, SEI growth has been reported to occur at a more positive potential range and to form a more effective passivating layer than at the basal plane.[16, 32] In addition, "blistering" has been noted in carbonaceous materials as a result of intercalation of solvent molecules into the graphite structure and their subsequent decomposition before enough protective SEI has been formed.[32, 38, 39] Thus, the formation of a stable and passivating SEI at a more positive potential would be beneficial.

While the presence of SEI is vital, it is difficult to control SEI formation and evolution, as the morphology, chemical composition, mechanical properties of SEI depend on several factors. A key factor to control SEI properties is the structure of the carbonaceous electrodes surface.[5, 8, 40, 41] It has been reported that the SEI on hard carbon (disordered carbon) contains more salt reduction products than solvent-reduction products, similar to the edge plane of HOPG and opposite to soft carbon and the basal plane of HOPG.[41] Several works also showed that on edge planes, the SEI forms more readily than that on basal planes, which might be due to the higher electrochemical activity of the edge planes.[5, 32, 39, 42, 43] Due to the heterogeneity of graphite electrode (containing both basal and edge planes), the SEI is not completely effective in passivating its surface. Strategies to improving the passivating property of SEI to protect graphite electrode from further reactions with electrolyte in subsequent cycles have long been pursued, such as coating the graphite with amorphous/disordered carbon.[44-47] Being more electrochemically active than the conventional graphite,[48] graphite surface with defects is expected to induce the SEI formation at a more positive potential and form a more effective SEI. Nevertheless, there has not been a systematic and fundamental study to understand how defects/disorder in carbon materials could affect SEI formation and evolution on the electrode surface during lithiation and delithiation processes.

Here, we report a systematic study that directly monitors and compares the formation and evolution of the SEI on both HOPG and a graphite electrode with defects, pseudo-graphite from University of Idaho thermolyzed asphalt reaction (GUITAR),[49] using complimentary characterizations of non-destructive operando EChem-AFM, *ex-situ* X-ray photoelectron spectroscopy (XPS), and computational modeling. Compared to

HOPG, GUITAR has a high concentration of defects and thus a more electrochemically active surface.[50] The onset potential of SEI formation at GUITAR (1.5V vs. Li/Li^+) is similar to the HOPG step edges (1.5V) and much more positive than HOPG basal plane (~0.8V). The lithium adsorption were found to be favored on a defected graphene surface from previous study than a defect free surface.[51-53] The reduction mechanism/adsorption of ethylene carbonate has also been investigated in existence of Li on defect free graphene and graphite.[54, 55] However, the theoretical study of reduction or adsorption of EC or $Li(EC)_n$ on a defected graphene/graphite were rarely done. In this work, with density functional theory (DFT) calculations, it is found that a graphene/graphite surface with defects (i.e., Stone-Wales (SW) and single vacancy (SV)) is preferred for EC-bonded Li compound adsorption. A model of SEI on the graphite with defects is proposed based on both operando EChem-AFM and *ex situ* XPS results. SEI formed on both HOPG and GUITAR has a mosaic-type structure with microphases of both inorganic and organic species. However, the SEI formed on GUITAR is more uniform, compact, denser, and thinner than that on HOPG. Moreover, in comparison with HOPG, the relative content of polymeric components is less than that of inorganic components in the SEI formed on GUITAR, while other organic components (e.g., alkyl carbonates and alkoxide) are almost negligible. In addition, the LiF content is much higher in the SEI on GUITAR than that on HOPG. It was shown that the SEI on GUITAR had negligible changes while at HOPG the SEI continued to grow upon the subsequent cycle, which suggests more effective passivation properties of the SEI formed on GUITAR that might be associated with its higher LiF content. This work compared topographic, mechanical, and chemical compositional evolution of the SEI formed on a graphite with (i.e., GUITAR) and without

(i.e., HOPG) defects. Our work provides insights of possible avenues to engineer effective SEI on carbonaceous electrode materials for better LIB performance.

2. Results and Discussion

2.1. Raman spectroscopy

Raman spectroscopy was carried out on HOPG and GUITAR sample to investigate the microstructural differences.[56] Graphitic materials usually display two characteristic peaks under visible laser excitation, the G band around 1560 cm^{-1} and the D band around 1360 cm^{-1}.[57] The G band is associated with the symmetric stretching of sp^2 hybridized carbon-carbon bonds, while the D band can be attributed to the sp^2 breathing mode arising from the structural defects.[56-59] As seen in **Figure 1**, HOPG only exhibited a single sharp peak at 1581 cm^{-1}, indicating a well-ordered graphitic structure. In contrast, a broad G band near 1582 cm^{-1} and a broad D band at 1353 cm^{-1} were observed for GUITAR samples, indicating the presence of defects. The peak intensity ratio between the D and G band was I(D)/I(G) = 1.12, further confirming a disordered structure for GUITAR.[60]

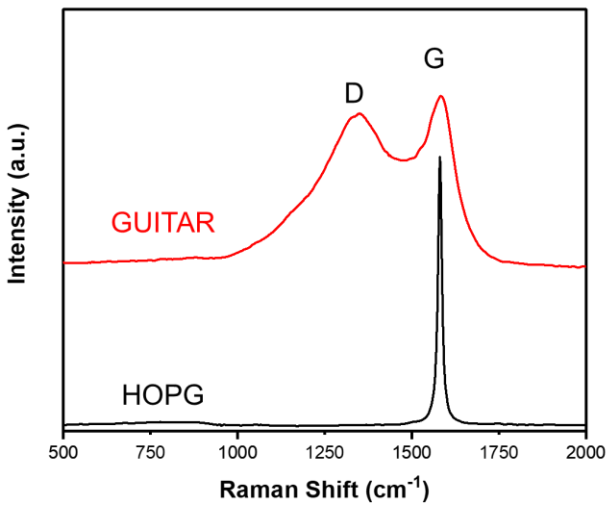

Figure 1. Raman spectra of pristine GUITAR and HOPG sample.

2.2. SEI formation and evolution on HOPG and GUITAR sample

Due to its environmental sensitivity, SEI analysis requires operations under inert and controlled environment. Therefore, operando EChem-AFM in an Ar-filled glove box was employed to study how structural defects in graphite electrodes affect SEI formation and evolution. Specifically, surface topographical changes of the HOPG and GUITAR sample were monitored during the first two cycles. **Figure 2** presents the SEI formation and evolution on an HOPG sample. Cyclic voltammogram (Figure 2a) was collected on the sample between open circuit potential (OCP, ~3 V) and 0.01 V vs. Li/Li^+, while concurrent AFM images were obtained. During the first cathodic scan (from OCP to 0.01V) on HOPG, a small current started to flow around 2 V, which can be assigned to the reduction of trace water or surface groups on HOPG, while the initial reduction of the electrolyte cannot be excluded.[37, 61, 62] The small hump observed between 1.5V to 1V can be assigned to the electrolyte reduction and initial SEI formation.[17] A pair of more prominent peaks appeared around 0.5 V with a discernible shoulder near 0.6 V. The shoulder at 0.6 V can be assigned to the intercalation of solvated Li^+ through the step edge of HOPG and the subsequential reduction of the intercalated solvent molecules between layers.[16, 17, 32, 35] While upon the second cycle, this shoulder disappeared, which indicates the absence of further solvated lithium-ion intercalation and its corresponding decomposition, possibly prevented by the SEI formed at the step edge during the first cycle. The peaks around 0.5 V can be assigned to the SEI formation on the basal plane, which did not vary significantly on the second cycle, indicating continuous SEI formation. The cathodic current rises significantly at 0.01 V, which could be ascribed primarily to the intercalation of lithium ions (forming LiC_6), while the anodic peak from 0.7 V to 1.7 V corresponds to the de-intercalation of lithium

ions.[22] The intercalation/de-intercalation potentialS of lithium ion are very similar in different electrolyte systems.[22, 61, 63, 64] Compared to the first cycle, the Coulombic efficiency improved during the second cycle, indicating the passivating behavior of the SEI at the electrode surface.

AFM image of the pristine HOPG sample is shown in Figure 2b. Several step edges were intentionally exposed, to evaluate the differences in SEI formation and evolution at different sites (i.e., basal planes vs. edge planes). The boxed regions highlight regions with prominent step edges, which show the presence of carbon terrace with step heights over 2.5 nm (corresponding to over 7 graphene sheets). The height profile is shown in **Figure S1** (Supporting Information). A series of operando AFM images of an HOPG sample during the first cathodic scan was shown in **Figure S2** (Supporting Information), from which the representative images with prominent changes were selected and presented in Figure 2c-2h. No topographic change was observed from OCP to 2 V (Figure S2, Supporting Information). Around 1.5 V, a small number of particles started to form, mainly along the step edges, especially in the boxed regions (Figure 2c). The particles formed in this potential range were ~0.3 μm in diameter. When scanned below 1.5 V, the SEI continued

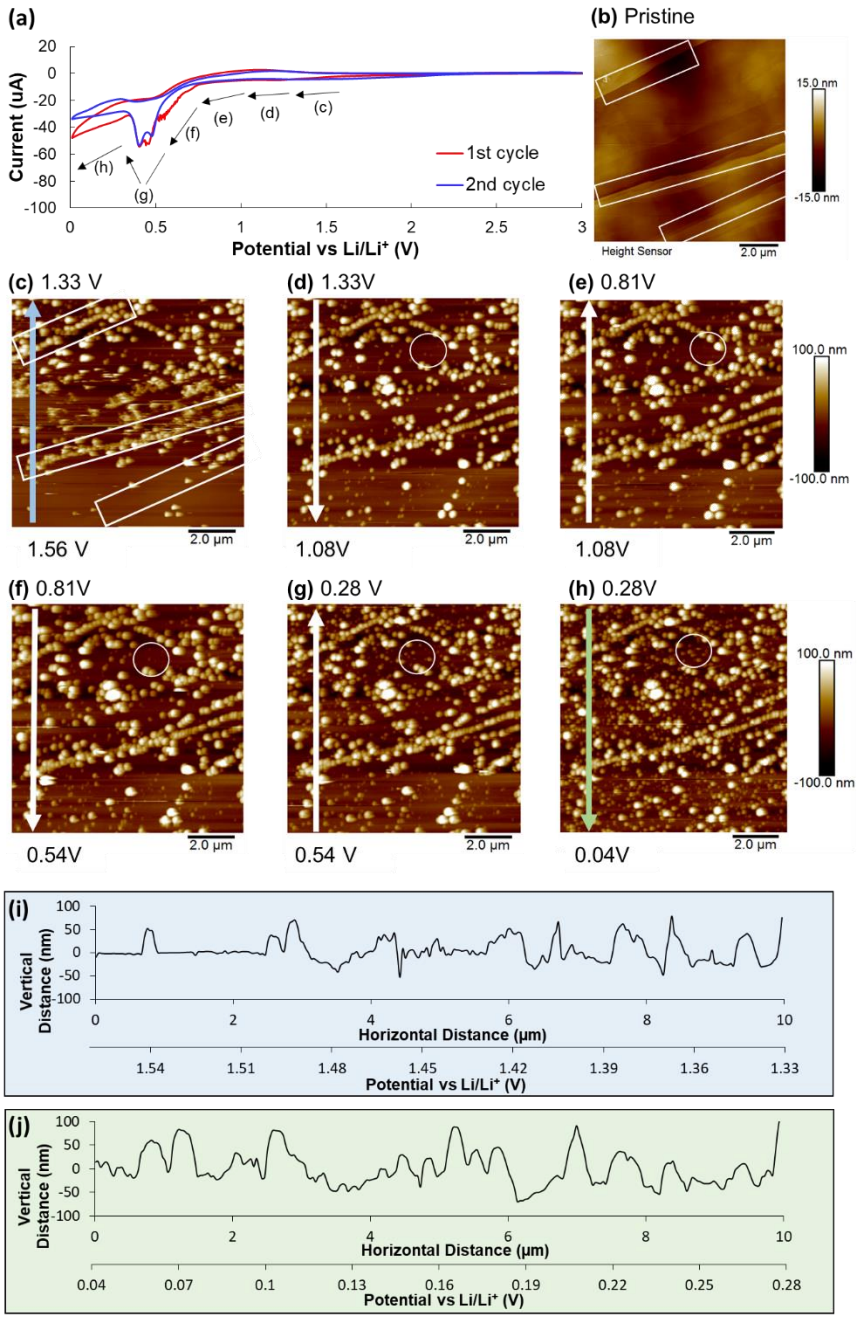

Figure 2. Operando EChem-AFM (10 µm x 10 µm) of an HOPG electrode in an electrolyte of 1.2 M $LiPF_6$ in EC: EMC (3:7 w/w), with a scan rate of 0.5 mV/s. (a) Cyclic voltammograms for the first two cycles of an HOPG electrode; the arrows indicate the potential range in which the corresponding AFM images were collected; (b) AFM image of a pristine surface of HOPG, boxed areas indicate ~10 layers of step edges; (c-h) Operando AFM collected during the cathodic scan of the first cycle at different potential ranges, the circled areas highlighted a small basal plane region; (i-j) representative height profile of (c) and (h) taken along the blue and green arrow, respectively.

preferential deposition at the step edges with a slightly larger average particle diameter of 0.5 μm (Figure 2c). This is concurrent with the small hump observed between 1.5 V and 1.0 V in CV. Thus, the current increase in this potential range can be attributed to the electrolyte decomposition and consequent SEI formation along the step edges. Upon further cathodic scan from 0.81 V to 0.54 V, a small number of SEI particles appeared on the basal plane (Fig. 2e). When scanned below 0.54 V, more particles formed across the surface. The diameter of SEI particles formed at the basal plane was smaller than 0.2 μm, as highlighted in the circled region (Figure 2f-2g). The initially formed SEI particles on the step edges have an average thickness of 80 nm, as estimated from the height profile (Figure 2h), which then slightly increased to 90 - 100 nm as the electrode was fully lithiated (Figure 2i). The particle on the basal plane were thinner, with an estimated thickness of 40 - 50 nm.

The SEI evolution observed on the basal plane of HOPG agrees well with previously reported results, in which the onset potential for SEI formation on the basal plane is around 0.7 V.[32-35, 37, 39] In comparison, SEI particles on the step edges formed at a more positive potential (1.5 V), with greater particle thickness and lateral particle size, as well as higher packing density than those at the basal plane, which corroborates well with previous report of preferential SEI formation on the step edges.[16, 22, 65, 66] However, a consensus has not yet been reached regarding the potential range in which SEI initially forms at the step edges of HOPG. Some have reported that SEI on the step edges forms below 1.6 V,[33] while others have reported formation below 1.0 V.[32, 39] Such variation in formation potential might arise from the crystallinity differences of the HOPG samples. In this study, we found that SEI formation on the step edges of HOPG began around 1.5 V, which agrees well with the *in-situ* AFM study by Xu et al.[16]

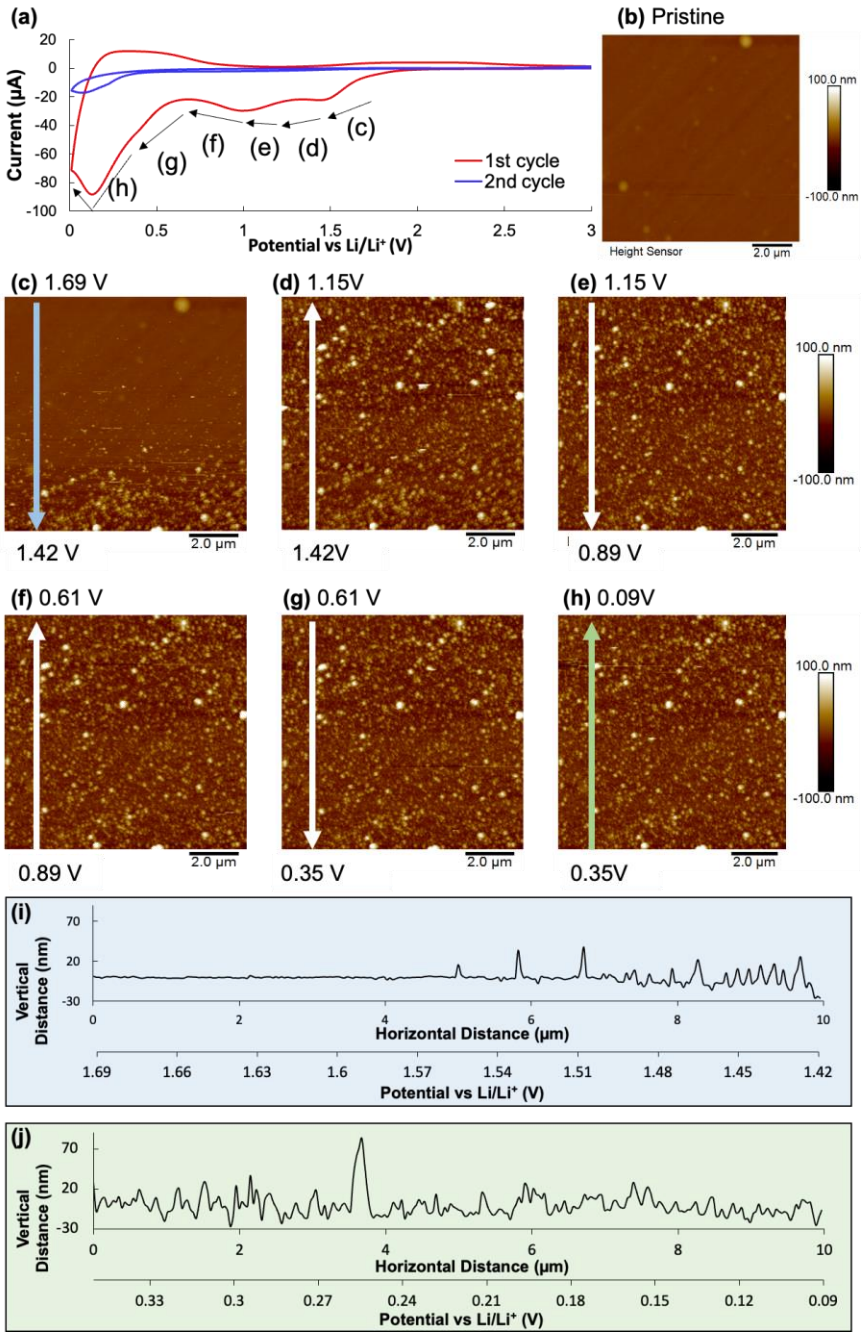

Figure 3. Operando EChem-AFM (10 μm x 10 μm) of an GUITAR electrode in an electrolyte of 1.2 M $LiPF_6$ in EC: EMC (3:7 w/w), with a scan rate of 0.5 mV/s. (a) Cyclic voltammograms for the first two cycles of an GUITAR electrode; the arrows indicate the potential range in which the corresponding AFM images were collected; (b) AFM image of a pristine surface of GUITAR; (c-h) Operando AFM images collected during the cathodic scan of the first cycle at different potential ranges; (i-j) representative height profile of (c) and (h) taken along the blue and green arrow respectively, plotted versus the corresponding potentials.

The SEI formation and evolution at the surface of the GUITAR sample were monitored under the same conditions as the HOPG sample (**Figure 3**). The chemical vapor deposition(CVD) process to synthesize the GUITAR thin film[49] allowed it to be coated on a large and flat surface (e.g., quartz with diameter of 2"), making it ideal for AFM imaging. Disordered carbon samples (e.g., hard carbon) had been investigated previously in the form of composite films (with binders and additives), which yielded low quality AFM images and complicated the interpretation of the EChem-AFM results.[34, 67] In this study, the thin film GUITAR without any binder or additive enables straightforward comparison of carbon surface w/o defects.

The cyclic voltammogram on a GUITAR sample is shown in Figure 3a, collected with the same parameters as HOPG sample (Figure 2a). Similar to the HOPG sample, the cathodic current on GUITAR also started to flow around 2 V and can be assigned to the reduction of water and surface groups, and possibly initial reduction of the electrolyte. [37, 61, 62] A small and shallow peak near 1.5 V upon further reduction is possibly associated with the onset of EC and EMC reduction with preferred reduction of EC.[17, 68, 69] A broad peak also appeared near 1 V, which has been reported for MesoCarbon MicroBeads (MCMB) graphite and hard carbon (HC) electrodes.[39] The peak can be assigned to further reduction of EC and EMC and concurrent SEI formation. It may also be associated with lithium-ion storage on the surface with defects, as described by Mochida et al.[70] A broad cathodic peak near 0.14 V is possibly associated with lithium-ion intercalation and additional electrolyte decomposition. An anodic peak appeared near 0.2 V, corresponding to the deintercalation of the lithium ions. In contrast to HOPG, the cathodic current from 2 V to 0.1 V on the second cycle decreased significantly relative to the first cycle of GUITAR,

indicating excellent passivating behavior of SEI formed from the first cycle. The peak at 0.14V on the second cycle also decreased compared to that on the first cycle, suggesting significant contribution of the irreversible electrolyte decomposition/SEI formation to the peak current on the first cycle. Nevertheless, it should be noted that this study is not to propose a new negative electrode material for lithium ion battery but to fundamentally understand the effect of surface defects at carbon electrode materials and to propose a possible coating material beneficial for a more stable and robust SEI.

Operando EChem-AFM was conducted at the surface of a GUITAR sample for comparison with the HOPG sample. For the pristine GUITAR (Figure 3b), unlike HOPG, no step edges were visible on the surface, which is consistent with previous SEM observations.[49] Around 1.5 V, small particles with diameter of ~0.1 μm started to from (Figure 3c). As it was scanned below 1.4 V, the SEI particles started to pack densely and uniformly, the lateral size of which did not change significantly. When the GUITAR sample was scanned below 1.15 V (Figure 3d-h), no significant topographic change was observed. Estimated from the height profile (Figure 3i-j), the SEI particle thickness was ~55 nm when initially formed, and almost remained the same as the electrode was fully lithiated. The SEI at GUITAR almost uniformly distributed across the electrode surface, while the SEI on HOPG exhibited variation in particle size and thickness due to the coexistence of the step edges and defect free basal plane.

The onset potential of SEI formation could be a measure of the electrochemical reactivity of the electrode surface. From our study, the order of the reactivity follows that: GUITAR (1.5V) ≈ HOPG edge plane (1.5V) > HOPG basal plane (below 0.8 V). Such finding agrees well with the previous study that the electrochemical activity of GUITAR is

similar to that of the HOPG edge plane while higher than the HOPG basal plane.[50] Similar phenomena have also been reported on other disordered carbon surface when compared to HOPG basal and edge planes.[39] Formation of a stable SEI at more positive potential can be beneficial to the reversibility of the graphite electrodes.[71] Moreover, the SEI formed on GUITAR is more homogeneous and much denser than HOPG, which provided a better coverage and consequently, a better passivation for the electrode as also supported by the 2nd-cycle CV.

2.3. DFT calculations — adsorption of EC, Li, and EC-Li

Provided that an effective adsorption should occur for further electrolyte reduction/decomposition, DFT calculations on both graphene and graphite were conducted to obtain a mechanistic understanding of how defect would influence the surface reactivity. We selected EC-Li structure as solvated lithium to simplify the system. Brønsted−Evans−Polanyi (BEP) relationship[72, 73] suggests that a more negative dissociation energy corresponds to a smaller activation energy, thus a more positive potential for EC decomposition. Thus the adsorption and dissociation/decomposition energies on defected and defect free materials are calculated to explain the experimental results. Graphite is modeled by three graphene layers[74-76]] and the reactions on single layer graphene is calculated as well. Pure EC adsorption was investigated first, and the results are shown in Figures S4 and S5 (Supporting Information). A more negative adsorption energy indicates a more stable configuration. Only molecular adsorption was predicted on defect free and Stone-Wales (SW) defected graphene and graphite and the optimizations for EC chemisorption structures were not successful; EC is predicted to be generally parallel to the basal plane (Figure S4, Supporting Information). The interactions are dominated by the

hydrogen bond between EC and the basal plane and the predicted physisorption energies are -0.55 to -1.27 eV for defect free and SW defected graphene, respectively. EC adsorption on a SW defect on graphene results a slight distortion of the basal plane. On graphite, the adsorption configurations are generally consistent to that on graphene and the adsorption energies are comparable. The calculated adsorption energies with EC perpendicular to the basal plane of graphene (0.33 eV on defect free and 0.39 eV SW defected surface) are weaker than the parallel adsorption mode (Figure S4, Supporting Information). Significantly different adsorption is predicted on a single vacancy (SV) defect and the results are shown in Figure S5 (Supporting Information). The chemisorption with the O in the C=O bond and the C in the carbonate group in EC bonded to two defective carbon atoms at an SV defect is more exothermic (-1.09 eV) than the physisorption with a parallel mode in graphene. Dissociation can take place as the breaking of a C-O bond from EC and the formation of a C-O bond with a defective carbon atom is predicted to be exothermic by 1.02 eV. The results on graphite are generally consistent with that on graphene with the energy difference less than 0.10 eV. The physisorption energy on defected free graphene and the chemisorption energy on SV defected graphene calculated with optPBE-vdw in the current work are comparable to the values calculated with PBE-D3.[77]

As the chemisorption of EC on the basal plane of defect free and SW defected graphite and graphene is not favored, the decomposition of EC itself on the surface would be least likely to occur. It has been reported that the presence of Li facilitates the reduction process of the EC.[54] We selected a model with an additional lithium atom after one-electron reduction of a Li^+ to study the reactions near the electrode under reduction conditions (the Li atom acts as an electron donor). For a direct comparison with defect free

and SW defected materials, EC adsorption/dissociation on SV defected materials is also studied with the presence of a Li atom.

The structures for the top and side views for EC-Li adsorption on graphene and the energetics for the stepwise Li and EC adsorption on graphene and graphite are shown in Figure 4. The adsorption energy of Li on graphene (-1.26 eV) is slightly less negative than that on graphite (-1.57 eV). The Li adsorption energy on the graphene with defect (-1.86 eV for an SW defect and -3.04 eV for an SV defect) is almost the same as on the defected graphite (-1.89 eV for a SW defect and -3.00 eV for a SV defect). Thus, the graphene layers do not affect much on the surface adsorption, and the existence of a defect results a stronger Li binding. In Li adsorption, there is a charge transfer from Li to surface carbon atoms and there is no extra spin on the Li adatom. Our calculated Li adsorption energies on graphene with and without a defect are consistent with the values calculated with PBE.[51, 52] Compared to that on a perfect surface, the SW defect lowers the adsorption energy of Li by 0.60 eV on graphene (0.32 eV on graphite) while the single vacancy lowers that by 1.78 eV for graphene (1.43 eV on graphite). EC adsorption on a Li pre-adsorbed surface is also shown in Figure 4. The chemisorption of EC takes place through the formation of a Li-O bond between the pre-adsorbed Li and the oxygen in the C=O bond of EC on defect free and SW defected surfaces. On an SV defect, the pre-adsorbed Li is bonded to both a =O and a -O atoms in EC. The EC adsorption on a Li pre-adsorbed surface is more exothermic than that on the clean surface without the presence of a Li and EC is stabilized by the pre-adsorbed Li through a charge transfer. Again, an SW defect lowers the EC adsorption by 0.50 and 0.11 eV for graphene and graphite. On a Li pre-adsorbed SV defect, EC adsorption energies are predicted to be -3.20 and -3.28 eV for graphene and graphite, respectively.

Apparently, the overall adsorption reaction (* + Li + EC → EC-Li*) on the defected materials are more exothermic than that on defect free materials and the exothermicities on different active sites follow the order of SV > SW > Defect Free. This is true for both graphene and graphite. We also calculate the adsorption energy of EC-Li as a complex on different materials and the exothermicities for EC-Li adsorption follow the same order (Figure 4). The more exothermicities range from 0.50 to 3.30 eV.

The products and energetics for EC decomposition are complicated, for example dependent on the anions in the electrolyte.[78] Here, EC-Li* decomposition with the formation of $LiCO_3$* and gas phase C_2H_4 is calculated without considering the anions to investigate the energetics on different materials. The results are shown in Figure S6 (Supporting Information). On defect free and SW defected materials, the Li is bonded to two -O atoms in a carbonate group in the surface $LiCO_3$*. On an SV defect, the Li is bonded to a -O atom and O=C=O in the surface $LiCO_3$*. C_2H_4 desorption energies are comparable on different surfaces and are predicted to be 0.35 to 0.50 eV. Again, the decomposition of EC (* + Li + EC → $LiCO_3$* + C_2H_4) on the defective surfaces is more exothermic than on the defect free by ~ 0.40 and 3.50 eV on a SW defect and a SV defect respectively. The difference of the decomposition energies on graphene and graphite are small.

Such significantly different adsorption and decomposition energies on defected and defect free carbon materials suggest a lower activation energy of EC decomposition on the defective carbon surface based on the BEP relationship. It also suggests that the voltage to drive the EC solvent decomposition would be more positive on a carbon surface with defects than on a defect free surface. This agrees well with the trend we observed from experimental results that on a carbon surface with defects (GUITAR), the SEI

formation/electrolyte decomposition occurs at a potential (1.5 V) more positively compared to that on a carbon surface without defect (basal plane of HOPG, below 0.8V).

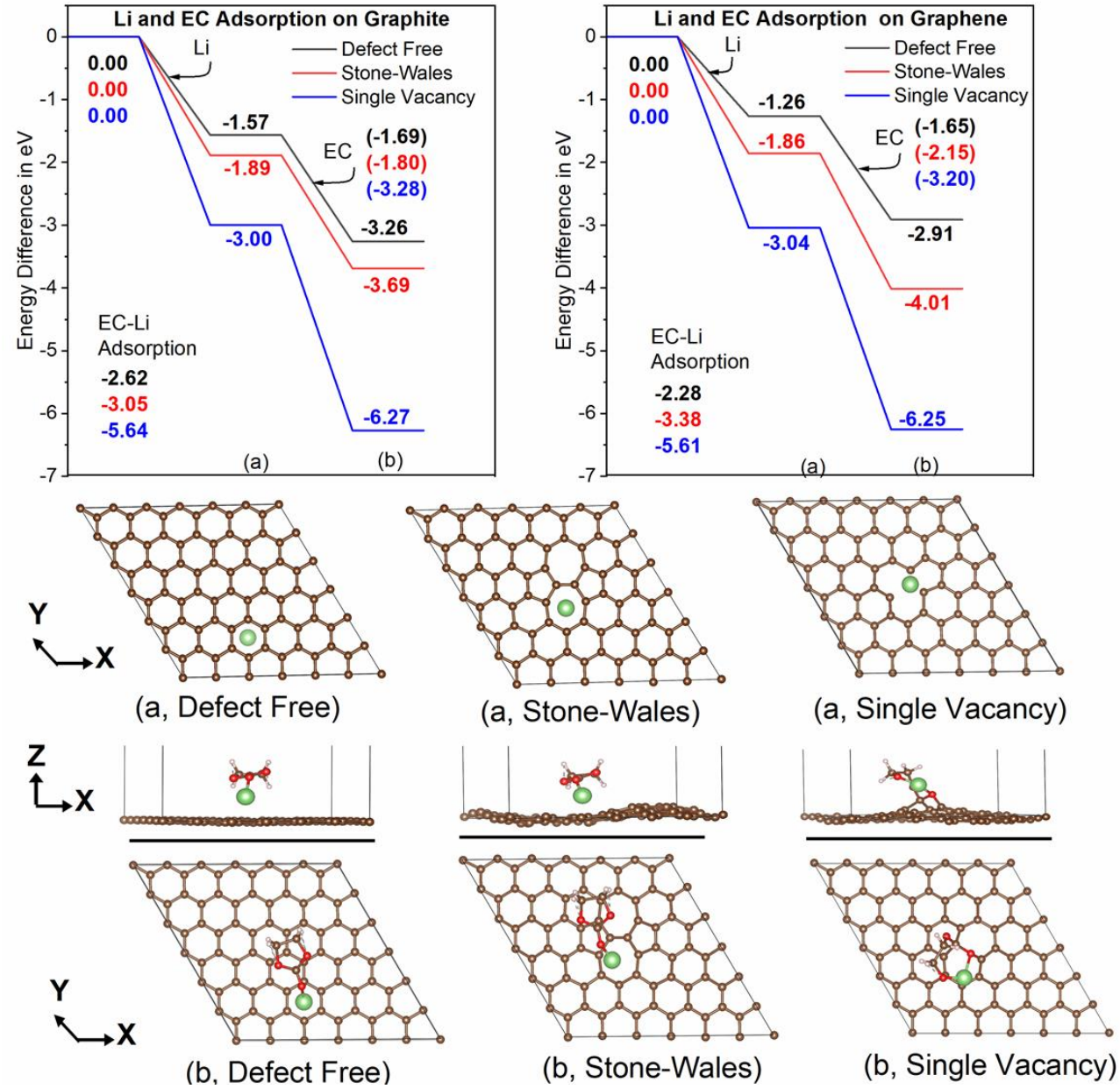

Figure 4. Relaxed structures and calculated Li (top view) and EC (both side and top views) adsorption energies (in eV) on the basal plane of defect free, SW defected, and SV defected graphene and graphite at the optPBE-vdw level. The values shown in the parenthesis are EC adsorption energies on Li pre-adsorbed surfaces. For clarity, only the structures on graphene are shown and the relaxed structures on graphite are similar to that on graphene. Lithium shown in green, carbon shown in brown, oxygen shown in red, and hydrogen shown in light grey.

2.4. Stability of SEI at HOPG and GUITAR sample after two full cycles

The stability of the SEI is critical for LIB performance. To evaluate the stability of the SEI formed on HOPG and GUITAR sample, a series of AFM images (25 μm x 25 μm, **Figure 5**) were collected at different potentials during the CV scan: pristine, end of the first cycle (at 3 V), turnover of the second cycle (around 0.01 V), and end of the second cycle (at 3 V). The root mean square (RMS) roughness (Rq) was used as a measurement of the topographic change. The pristine HOPG sample appeared to be very smooth and flat with an average surface roughness of the basal regions as 1.0 nm (Figure S7a, Supporting Information). At the end of the first cycle, the roughness of the basal regions increased to 32.9 nm (Figure S7b, Supporting Information) due to the SEI formation, which further increased to 38 nm (Figure S7c, Supporting Information) after being scanned to 0.01 V at the end of the cathodic scan in the second cycle and 41.6 nm (Figure S7d, Supporting Information) at the end of the second cycle. The surface roughness significantly increased upon the second cycle, especially in the vicinity of the step edges (Figure 5b-d). Such increase could be attributed to either further SEI growth or appearance of the blisters (due to co-intercalation of solvated Li^+) underneath the graphite layer. In either case, the SEI formed during the first cycle did not provide sufficient protection over the electrode from further reaction with the electrolyte upon cycling. In contrast, no significant topographic change, was observed on GUITAR surface once the SEI was formed after the first cycle (Figure 5e-h), indicated by nearly constant surface roughness of 16-17 nm. The result suggests that the SEI on GUITAR formed during the first cycle effectively passivated the electrode surface and was very stable upon the second cycle. This result corroborates well with the CV study on GUITAR, which demonstrated a significant reduction in the cathodic

current during the second cycle. Such good stability and passivating ability of the SEI formed on GUITAR might be associated with uniformity of the SEI, the chemical compositional difference and mechanical difference induced by the defect sites on GUITAR.

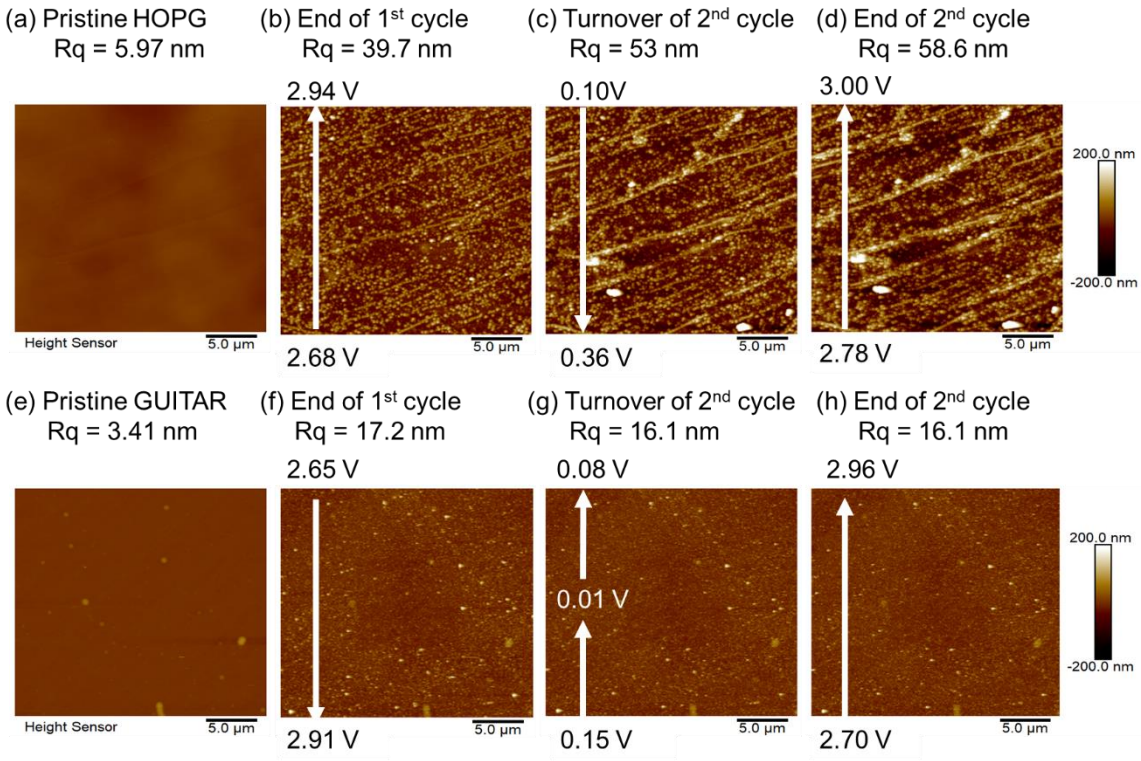

Figure 5. AFM images (25 µm x 25 µm) of HOPG: (a) in its pristine state; (b) at the end of the first cycle (nearly delithiated, at 3V); (c) around the turnover potentials of the second cycle, (nearly fully lithiated, image collected while scanning from 0.10V to 0.36V) ; (d) at the end of second cycle (fully delithiated, at 3V); and GUITAR (e) in its pristine state; (f) at the end of the first cycle; (g) around the turnover potentials of the second cycle, (image collected while scanning cathodically from 0.15 V to 0.01 V then anodically to 0.08 V); (h) at the end of the second cycle.

2.5. Chemical compositional evolution of SEI on HOPG and GUITAR electrode during the first cathodic scan

Complimentary to the operando EChem-AFM, *ex-situ* XPS was conducted to investigate the chemical composition changes of the SEI formed on HOPG and GUITAR

samples at different potentials (**Figure 6**). Figure 6a presents the high-resolution C 1s, O 1s, Li 1s, and F 1s core XPS spectra for the HOPG sample before and after being scanned from OCP to different potentials. Due to the spot size limitation of XPS, it is difficult to differentiate step edges from the basal plane on HOPG. To mitigate this, the exposure of the step edges was minimized during cleaving the HOPG surface, leading to the response mainly from the basal plane. For pristine HOPG, the characteristic graphite (i.e., sp^2) peak (284 eV) and a satellite peak (π-π*, 290.5 eV) were observed in the C 1s spectrum.[79] The intensity of the graphite peak decreased with lithiation, indicating the electrode surface was gradually covered by the SEI. When the HOPG electrode was scanned from OCP to 2 V and 1.5 V, additional peaks were observed in the C 1s spectrum, which can be assigned to C-O-C (286-287 eV) and C=O bonds (289.9-290.9 eV). Likewise, in the O 1s spectrum, a peak appeared near 533.3 eV, which can be assigned to C=O bond. At potentials above 1.5 V, barely any Li 1s or F 1s peaks were observed, which suggested that instead of SEI formation, the chemical species at the HOPG surface might be from solvent adsorption (e.g., ethylene carbonate).[80-82] The XPS results corroborate well with the EChem-AFM results (Figure 2), which indicated that almost no SEI is formed above 1.5 V. When the potential was scanned further to 1 V, the presence of polyethylene oxide (PEO)-type polymers (C 1s: 286.5eV and O 1s: 534 eV),[83-85] and alkyl carbonate (C 1s: R–***C***H_2OCO_2-, 287.7 eV and R–CH_2O***C***O_2-, 289.2 eV)[85] suggests the reduction of the carbonate solvents, as well as the possible polymerization of EC.[86] A small amount of $LiPF_6$ (F 1s: 688 eV, Li 1s: 58 eV) was also observed, indicating the salt might be trapped in the polymeric structure. Upon further cathodic scan to 0.5 V, lithium alkoxide (R-O-Li) (C 1s: 283 eV, O 1s: 532 eV),[87, 88] lithium fluoride (LiF) (F 1s: 684.5 eV, Li 1s: 55.4 eV)[37] and

$Li_xPO_yF_z$ (F 1s: 687 eV, Li 1s: 57.9 eV)[85, 89, 90] started to form on the electrode surface. However, Li_2CO_3 and lithium alkyl carbonate formation cannot be ruled out due to the presence of carbonate peaks in the C 1s spectrum (R–$CH_2O\boldsymbol{C}O_2$-, 289 eV and CO_3^{2-}, 290.3 eV). LiF and $Li_xPO_yF_z$ are common SEI component when $LiPF_6$ is present in the electrolyte,[63, 83, 91, 92] while Li_2CO_3 and lithium dicarbonate $(CH_2OCO_2Li)_2$ can be found in SEI formed in EC-based electrolytes and lithium alkoxide (R-O-Li) is found as a reduction product when dimethyl carbonate (DMC) or ethyl methyl carbonate (EMC) is present in the electrolyte.[93] After the potential was scanned to 0.01V, a small amount of Li_2CO_3 (Li 1s: 56.5 eV and C 1s: 290.3 eV) and lithium alkyl carbonate (C 1s: R–$\boldsymbol{C}H_2OCO_2$-, 287.7 eV and R–$CH_2O\boldsymbol{C}O_2$-, 289.2 eV) were found along with polymeric deposits (C 1s: C-O 286.2 eV and O 1s: 535.5 eV). Peaks in the Li 1s spectrum (59.4 eV) and F 1s spectrum (688.7 eV) might be from more $LiPF_6$ adsorption or its decomposition product Li_xPF_y.[21, 64, 89] The XPS results suggest that SEI starts to form on the surface of HOPG around 1 V with the major components being polymers. Inorganic SEI species begin to form around 0.5V, but with the polymeric components still dominating.

The high-resolution XPS spectra of GUITAR subject to the same electrochemical conditions as HOPG sample are shown in Figure 6b. On the pristine GUITAR surface, sp^2 C (284.1 eV, 85%) and sp^3 C (284.9 eV, 15%) peaks are present in the C 1s spectrum, consistent with previous finding.[48] As the potential was scanned to 2 V, additional small peaks (286.5 eV and 289.5 eV) appeared in the C 1s spectrum along with a new peak in the O 1s spectrum (533 eV). As with the HOPG sample in a similar potential range, these peaks can be attributed to solvent adsorption. In addition, a small amount of $LiPF_6$ adsorption was detected in the Li 1s (57.6 eV) and F 1s spectra (687 eV). The result indicates no electrolyte

decomposition occurred above 2 V, in agreement with the CV study (Fig. 2a), where almost no cathodic current was observed in the corresponding potential range. After the potential was scanned to 1.5 V, PEO-type polymers (C 1s: 286.3 eV and O 1s: 533.7 eV) and $LiPF_6$ (F 1s: 687.4 eV, Li 1s: 58.4 eV) were observed as the major components, along with a small amount of lithium alkyl carbonates (C 1s: R–***C***H_2OCO_2-, 287.8 eV and R–CH_2O***C***O_2-, 289.3 eV). When the potential was scanned to 1 V, the composition of SEI remained the same as that formed at 1.5V. The lower graphite peak in the C 1s spectrum indicated a higher coverage of SEI on the electrode as the potential was scanned to a more negative region. After the potential was scanned to 0.5 V, lithium alkoxide (R-O-Li) (C 1s: 282.8 eV, O 1s: 531.8 eV) appeared on the surface of GUITAR along with increasing concentration of lithium alkyl carbonates. In addition, the peaks indicative of $LiPF_6$ (F 1s: 687.4 eV, Li 1s: 58.4 eV) almost disappeared, concurrent with the appearance of LiF (Li 1s: 55.8 eV, F 1s: 685 eV) and $Li_xPO_yF_z$ (F 1s: 687.6 eV, Li 1s: 57.3 eV) peaks. At 0.01V, LiF (Li 1s: 55.4 eV, F 1s: 684.5 eV) and polymers (C 1s: 284.7 eV) were the dominant components, with a small amount of $Li_xPO_yF_z$ and lithium alkyl carbonates (O 1s: 532.5 eV) also present. On the GUITAR sample, the SEI started to form around 1.5 V, which is more positive than the onset potential of SEI formation on HOPG basal plane (below 1.0V) and consistent with operando EC-AFM results. On both GUITAR and HOPG sample, the organic components dominated the electrode surface at the initial state of SEI formation, while the salt decomposition products began to form around 0.5V. At 0.01V, the SEI on GUITAR contains relatively more inorganic contents, specifically LiF, compared to the SEI on HOPG. It is noteworthy that no Li_2CO_3 was observed in the

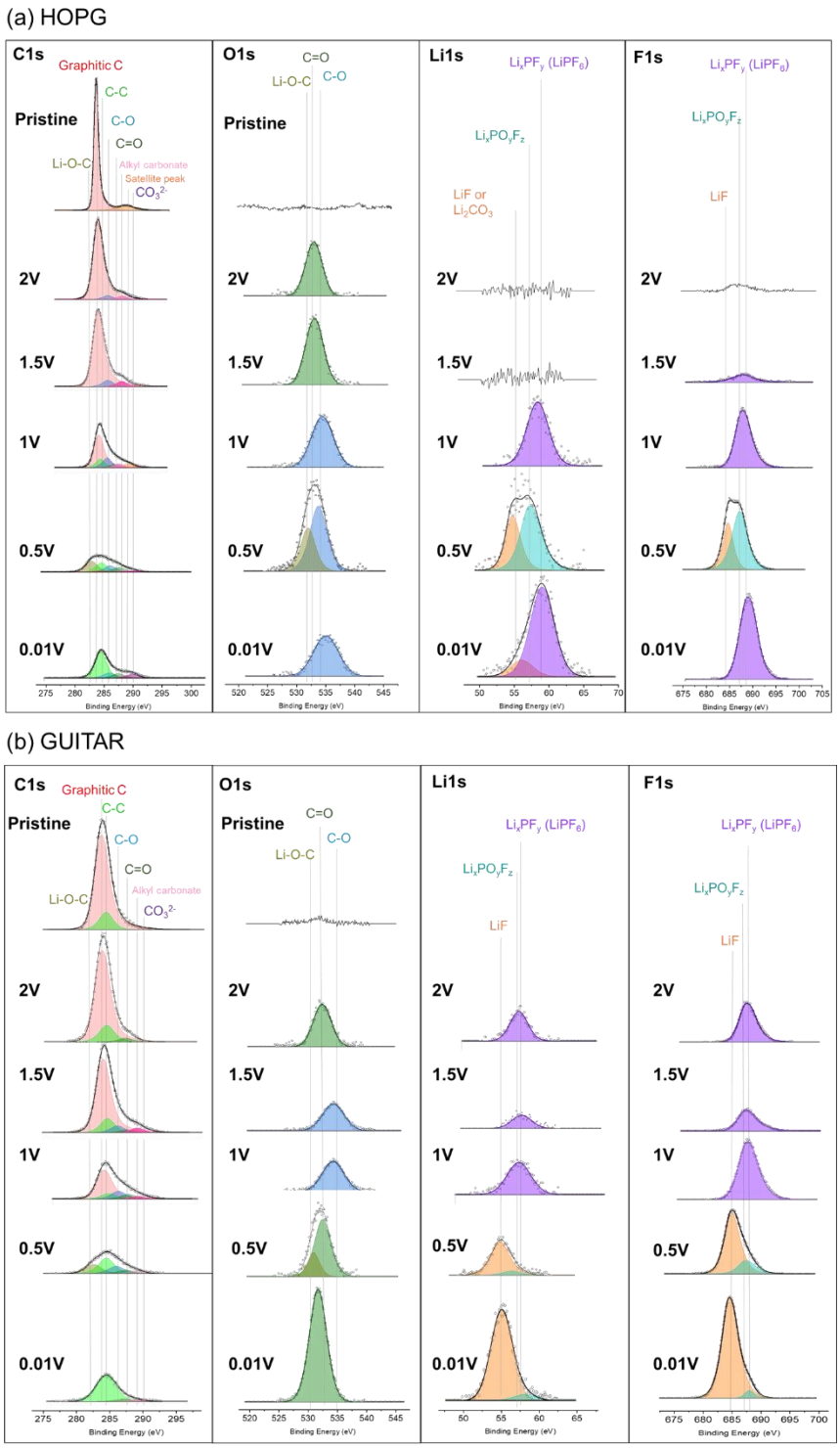

Figure 6. High resolution XPS spectra of C 1s, O 1s, Li 1s, F 1s in (a) HOPG and (b) GUITAR electrodes scanned through the potential ranges as indicated.

SEI formed on GUITAR. Such finding is consistent with Peled's previous report that Li_2CO_3 was only observed in SEI formed on HOPG basal plane, but not on HOPG edge

plane or practical soft and hard carbons.[41] LiF-rich SEI has been found to effectively suppress the Li dendrite formation due to the high interfacial energy against Li and improve the Li metal electrode cyclability,[94, 95] facilitate Li dendrite suppression,[19] high temperature cycle performance,[96] and received growing recognition lately.[19] Approaches to artificially enrich the SEI with LiF has also been reported.[97] On GUITAR, a graphite with defects, LiF is readily present in the SEI, which could be beneficial for long-term stability and can lead to a new approach to design the SEI on graphitic electrode materials. The graphitic coating with defects can also be applied to the Li metal and other high capacity electrodes for a stable SEI formation.

2.6. SEI formation and evolution mechanisms at HOPG and GUITAR electrode during the initial lithiation process

Previous studies have reported either *ex-situ* XPS of SEI formed at different potentials[89] or the depth profile of SEI formed on the fully lithiated/delithiated electrodes.[98, 99] However, compositional evolution of the bulk SEI at different potentials is also important to understand the SEI formation and evolution mechanisms, which has not been reported yet to the best of our knowledge. In this work, we fill this gap by investigating the high-resolution depth dependent XPS spectra of SEI formed at different potentials on both HOPG and GUITAR electrode. It is noteworthy that the monoatomic Ar^+ bombardment will affect the chemical state of elements and the sputtering will in turn alter the stoichiometry of chemical species to a great extent. In terms of responses to Ar^+ bombardment, inorganic compounds are less susceptible under ion irradiation damage compared to organic species. Hence, we limit our discussion here to lateral composition of

the SEI at the surface based on XPS results from Section 2.4 and the trend of the depth-dependent distribution of inorganic SEI components along the thickness of the SEI.

$$LiPF_6 \rightleftharpoons LiF \downarrow + PF_5 \uparrow \quad \text{(R1)}$$

$$nEC \xrightarrow{PF_5} (-CH_2CH_2-O-)_n \downarrow + nCO_2 \uparrow \quad \text{(R2)}$$

$$2EC + 2Li^+ + 2e^- \rightarrow (CH_2OCO_2Li)_2 \downarrow + C_2H_4 \uparrow \quad \text{(R3)}$$

$$2EMC + 2Li^+ + 2e^- \rightarrow$$

$$CH_3OCO_2Li \downarrow or\ CH_3CH_2OCO_2Li \downarrow + C_2H_6 \uparrow or\ (CH_3CH_2)_2 \uparrow \quad \text{(R4)}$$

$$PF_5 + H_2O \longrightarrow 2HF + PF_3O \quad \text{(R5)}$$

$$PF_3O + xLi^+ + xe^- \rightarrow xLiF \downarrow + Li_xPOF_{3-x} \downarrow \quad \text{(R6)}$$

$$ROCO_2Li \rightarrow ROLi \downarrow + CO_2 \uparrow (\text{R} = \text{methyl or ethyl}) \quad \text{(R7)}$$

$$(CH_2OCO_2Li)_2 \rightarrow (CH_2OLi)_2 \downarrow + CO_2 \uparrow \quad \text{(R8)}$$

$$EC + 2Li^+ + 2e^- \rightarrow Li_2CO_3 \downarrow + CH_2 = CH_2 \uparrow \quad \text{(R9)}$$

$$(CH_2OCO_2Li)_2\ or\ 2ROCO_2Li + H_2O \rightarrow$$

$$Li_2CO_3 + (CH_2OH)_2 \text{ or } 2ROH + CO_2 \uparrow \quad \text{(R10)}$$

$$PF_5 + xLi^+ + xe^- \rightarrow xLiF \downarrow + Li_xPF_{5-x} \downarrow \quad \text{(R11)}$$

Above reactions (R1-11) present possible steps associated with the SEI formation. Based on the XPS and EChem-AFM results, we propose the SEI formation and evolution at HOPG and GUITAR electrode during lithiation in **Figure 7**. The possible reactions at difference potentials are also proposed in the following discussion. The modulus results

were collected simultaneously with the AFM image and are also presented to qualitatively illustrate the mechanical property evolution of SEI.

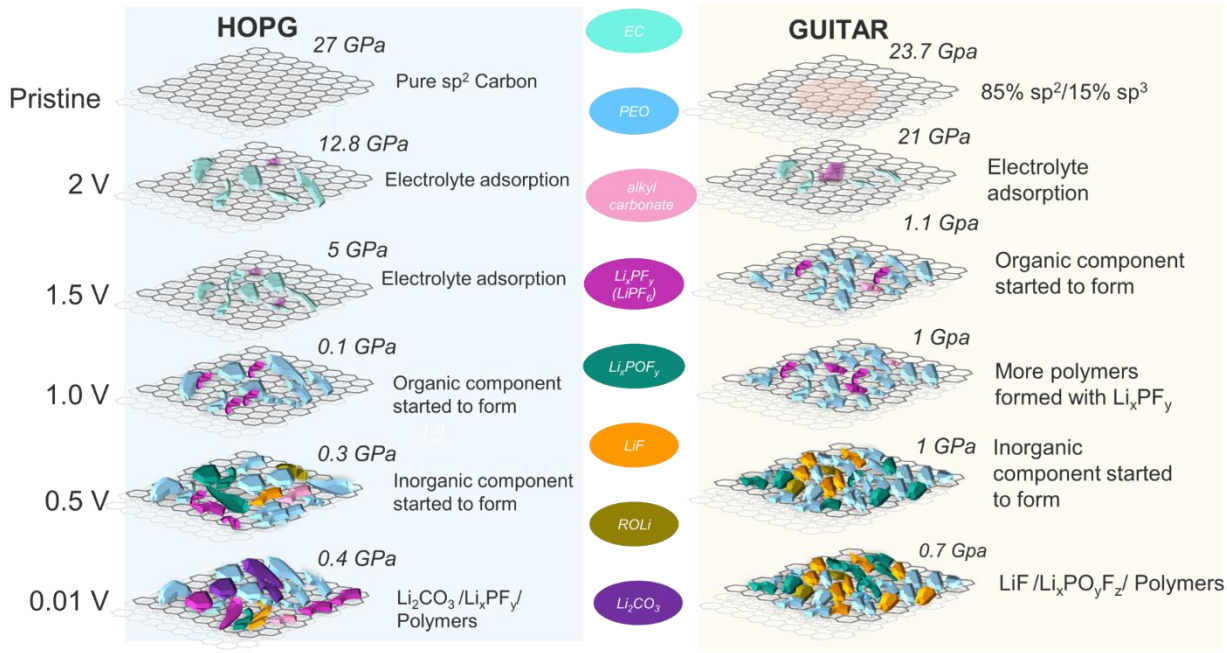

Figure 7. Scheme of the compositional distribution and mechanical property of the SEI on HOPG and GUITAR sample at different potentials.

The high-resolution depth dependent C 1s, Li 1s and F 1s XPS spectra of HOPG sample cathodically scanned to different potentials are presented in **Figure 8**. Polymers and lithium alkyl carbonate start to form below 1V, with polymers dominating among the SEI components. The chemical and thermal instability of salt $LiPF_6$ leads to an equilibrium show in R1, as summarized in Xu's review.[100] The decomposition product PF_5 tends to initiate the ring-opening polymerization as in R2, which leads to the polymeric deposition, in the presence of non-aqueous electrolytes.[101, 102] The EC undergoes a two electrons reduction reaction and forms the lithium alkyl carbonate as in R3, which was first reported by Aurbach.[103-105] One more possible source for the alkyl carbonate is the decomposition

production of EMC, as in R4.[69] The measured modulus significantly decreased from 27 GPa as of the pristine surface to 0.1 GPa at 1V. Such difference can be attributed to the soft nature of the polymeric and organic SEI. It is also noted that the electrolyte salt adsorbs at the electrode surface, possibly surrounded by the organic SEI components, as shown in Figure 8a. The PF_5, as the decomposition product of $LiPF_6$, which later reacts with trace amount of water to form additional LiF and PF_3O, as in R5. When the potential is scanned to 0.5V, the reduction of PF_3O yields $Li_xPO_yF_z$ (R6).[105, 106] It is noteworthy that LiF only exists at the surface of the SEI, while the $Li_xPO_yF_z$ predominates the inorganic SEI components throughout the bulk of the SEI. Concurrently, lithium alkyl carbonates precipitate and further decompose to lithium alkoxide (R7-8). Li_2CO_3 is also observed and could be formed in a few possible pathways. When the concentration of EC is low, it could be a direct product of EC decomposition, as in R9.[26, 54, 103, 104] However, such pathway does not likely occur since the EC concentration is pretty high in the used electrolyte system (EC:EMC = 3:7 by *wt%*). It could possibly be a result of the alkyl carbonate reacting with the trace amount of water, as in R10.[69, 105] After the potential being scanned below 0.5V, the content of the inorganic components in SEI increases, which can also be confirmed by the increased modulus (0.3 GPa).

The presence of only the graphite peak (284 eV) in C 1s spectra and disappearance of other C 1s peaks and Li 1s and F 1s peaks are indicative of a complete SEI removal and exposure of the native graphite electrode surface after Ar^+ sputtering. Thus, the sputtering time required for SEI removal can be correlated to the SEI thickness, which reaches the maximum at fully lithiated state (0.01V), as shown in **Table S1** (Supporting Information). At 0.01V, Li_xPF_y exists at the surface of the SEI along with small amount of LiF, as

reduction products of PF_5 (R11) as well as small amount of Li_2CO_3 as a possible product of lithium alkyl carbonate reacting with water (R10). $Li_xPO_yF_z$ still dominates the SEI closer to the electrode surface. The modulus increased slightly to 0.4 GPa, which is possibly a result of more inorganic components precipitation.

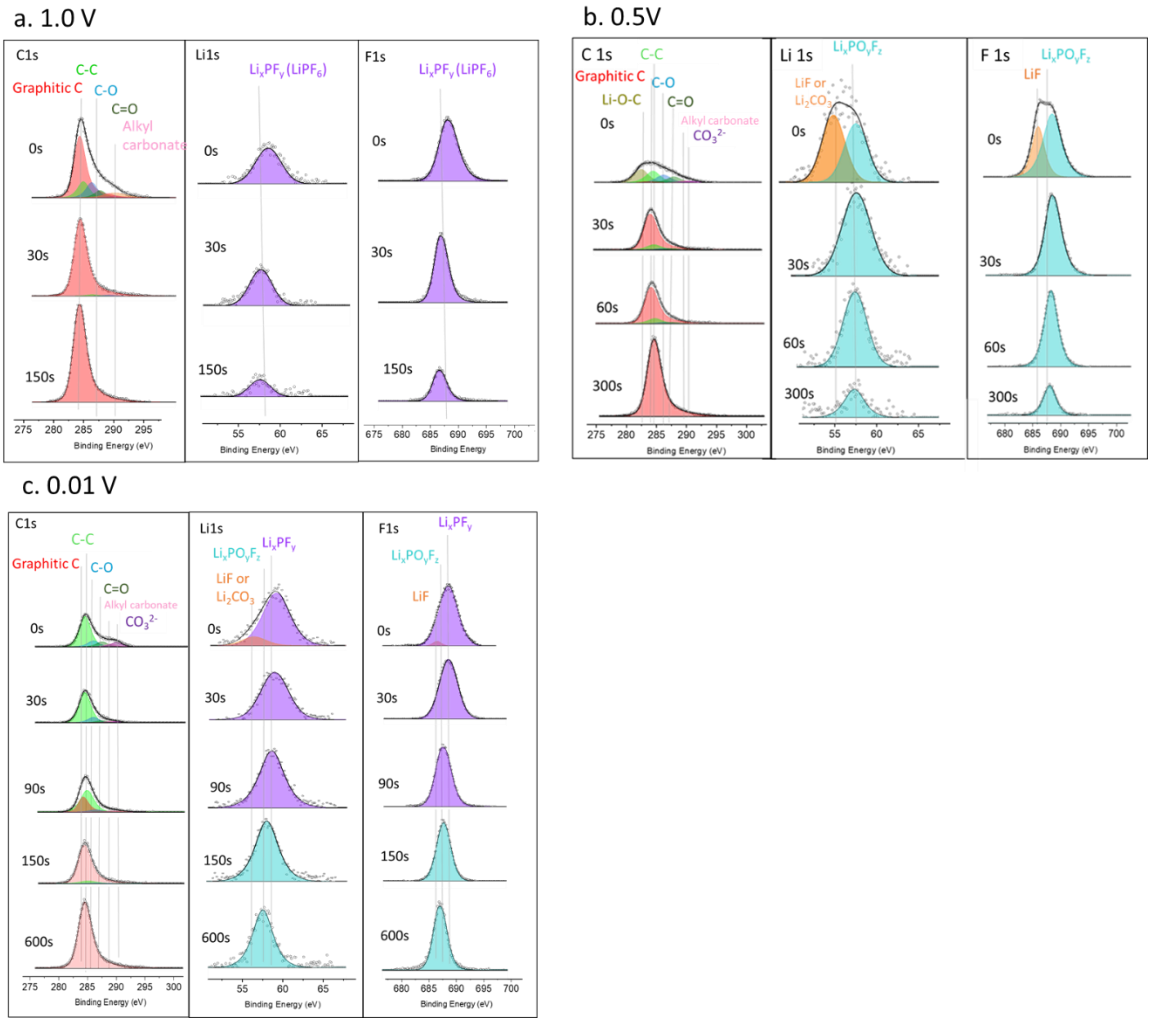

Figure 8. High resolution XPS spectra of C 1s, O 1s, Li 1s, F 1s before and after Ar ion sputtering in SEI formed on HOPG which has been scanned from OCP to 1V, 0.5V and 0.01V vs Li/Li^+.

The depth dependent XPS spectra of GUITAR subject to the same electrochemical conditions as HOPG sample are shown in **Figure 9**. On the GUITAR electrode, the SEI

started to form around 1.5 V (Figure 9a), but with similar SEI components distribution to that at HOPG electrode (albeit at 1 V). Similarly, the modulus also decreased from 23.7 GPa on the pristine surface to 1.1 GPa, due to the appearance of polymer and alkyl carbonate as products from decomposition of EC and EMC (R1-4). When the potential was scanned to 1 V (Figure 9b), the SEI comprised almost the same components with slightly different distributions (with similar modulus of 1 GPa) as at 1.5V and more EMC reduction and decomposition products (R4, R7). Upon reduction to 0.5 V, LiF dominated the inorganic components at the SEI surface with $Li_xPO_yF_z$ dominating the inorganic components in the bulk SEI (R5-6). Increasing contents of polymeric products and lithium alkyl carbonates were observed with lithium alkoxide (R-O-Li) as a product of lithium alkyl carbonate decomposition (R7). A significant difference was observed in the SEI at GUITAR sample as compared to HOPG sample: no Li_2CO_3 was observed. This is in agreement with previous reports that carbonates can only be observed in the SEI formed on HOPG basal plane, instead of HOPG edge plane, soft and hard carbons.[41] At 0.01V, LiF still presents and dominates the inorganic components at the top layer while $Li_xPO_yF_z$ dominates the bottom layer. LiF is much more enriched in the SEI on GUITAR compared to that on HOPG. One hypothesis to explain the LiF enriched SEI and the Li_2CO_3 absence on GUITAR is that LiF deposits on GUITAR more uniformly and densely at the SEI surface compared to HOPG, which sufficiently protected the SEI components (e.g., lithium alkyl carbonate) from exposure to moisture. It has been reported that LiF was introduced to the solid electrolyte synthesis to suppress the Li_2CO_3 formation[107] and functioned as a SEI component with a good passivating ability on Li and Si electrodes.[94, 95] The LiF-rich SEI formed on GUITAR could also explain the good stability exhibited upon cycling, as

shown in Figure 5. The role of LiF in SEI and its impact on the electrochemical performance of LIB remain under debate.[19] Despite that LiF has an electron insulating nature and a low ionic conductivity (~10^{-13} – 10^{-14} S cm^{-1}),[108] it exhibits high mechanical strength, low

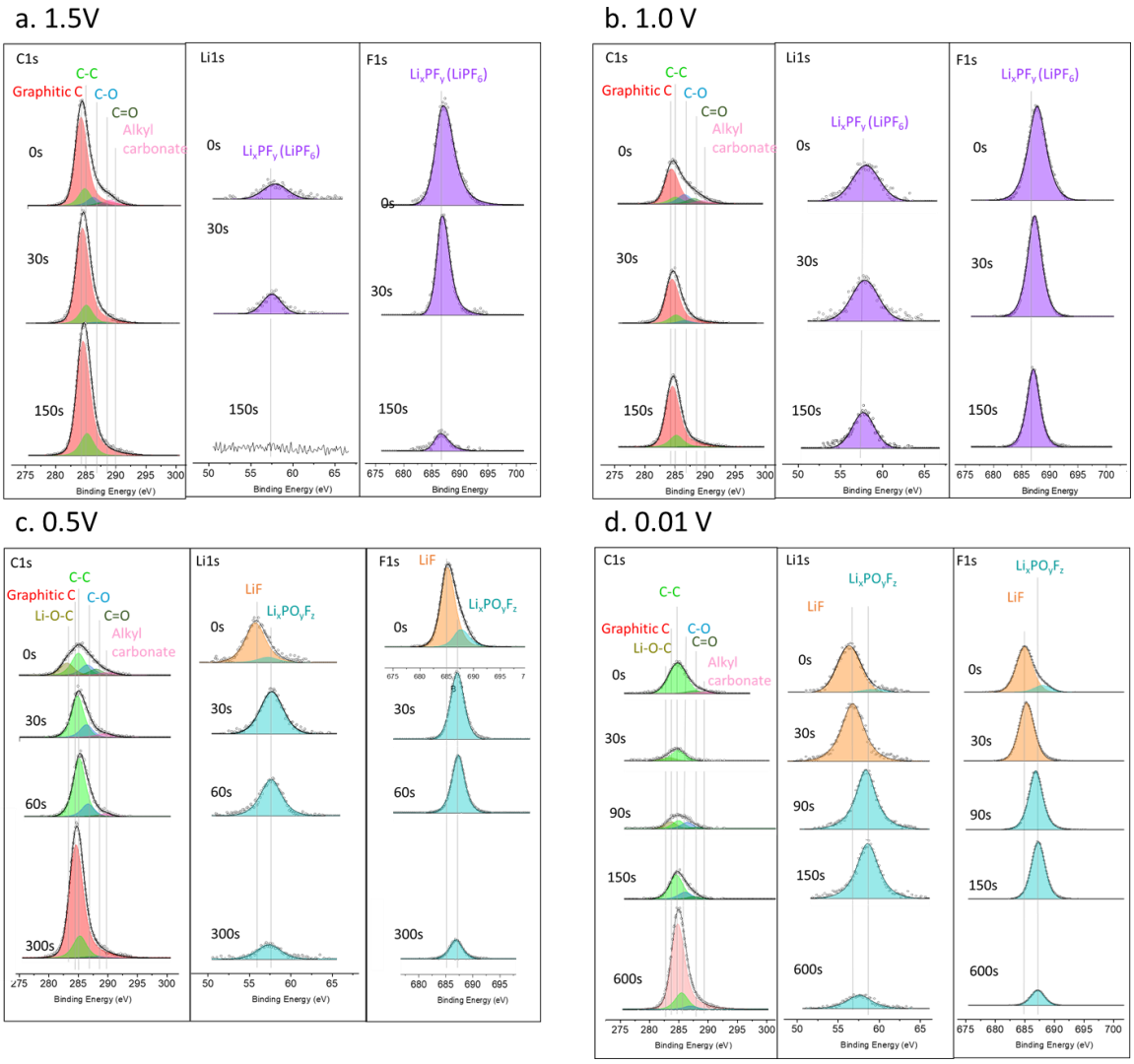

Figure 9. High resolution XPS spectra of C 1s, O 1s, Li 1s, F 1s before and after Ar ion sputtering in SEI formed on GUITAR which has been scanned from OCP to 1.5V, 1.0V, 0.5V and 0.01V vs Li/Li^+.

solubility, wide band gap, which prevent electron leakage making it a suitable SEI component.[109, 110] LiF enriched SEI was reported to play an important role in regulating the homogeneous deposition of Li^+ ions.[111, 112] Furthermore, $Li_xPO_yF_z$ was reported to

prevent the transition metal deposition and effectively suppress the rollover failure for LIBs in a recent study.[113] At the fully lithiated state (0.01V), the SEI on GUITAR contains more $Li_xPO_yF_z$ than that at HOPG, which further promotes a stable SEI formation.

3. Conclusion

We compared the SEI formation and evolution on both HOPG, representing the graphite deficient of defects, and GUITAR, representing the graphite with defects utilizing operando EChem-AFM, *ex-situ* XPS, and DFT calculations. The SEI forms more readily at the graphite with defects compared to the HOPG. The DFT calculations help explain such phenomenon: the adsorption energy barrier of the EC bonded Li compound is much lower on a graphite surface with defects compared to that without defect, which could lead to a lower decomposition energy barrier and thus a more positive onset potential. The defects in the graphite structure induce formation of a thinner, denser and more uniform SEI on the electrode. The SEI at the graphite with defects also exhibits a stronger passivating ability and a good stability upon cycling. The SEI formed on the graphite with defects was rich in LiF, which has been reported as an effective passivating component in SEI on Li and Si electrode materials. Moreover, the high shear modulus of LiF enables a robust protection over the anode materials from pulverization for enhanced cycling stability. In addition, the higher $Li_xPO_yF_z$ content in SEI of GUITAR can assist suppression of rollover failure for LIBs. Thus, the graphite with defects can be designed as coatings onto other high-capacity electrodes such as Li, Si, and Sn, for a stable SEI. Furthermore, the graphite with the defects can be coated onto the conventional graphite electrodes to improve its rate performance and cycling stability for applications such fast charging batteries. Our study provides a fundamental understanding of SEI formation and evolution on graphite electrode materials

with and without defects, which offers a new design strategy of engineered SEI for high performance LIB and beyond.

4. Experimental methods

Raman Spectroscopy: Raman spectra were acquired with a Horiba LabRAM HR Evolution Raman microscope (Irvine, California) using a 532nm excitation laser and 600 gr/mm grating with signal accumulations of three 30s scans. After instrument calibration, samples were scanned at room temperature under ambient conditions. The incident laser power was 100 mW, and samples were viewed at a magnification of 50x. Scattered light was collected with a thermoelectrically cooled Si CCD detector. Data was acquired using the LabSpec 6 Spectroscopy Suite software. Spectral peak fitting was performed in OriginPro software, with Gaussian_LorenzCross mode until a correlation of 0.99 was found and the curve converged.

GUITAR sample preparation: GUITAR samples were prepared via a chemical vapor deposition (CVD) method.[48] The tube furnace was heated to a temperature of 900 °C and the carrier gas (N_2) purifier was preheated to 400 °C in a gas chromatograph gas purifier oven (Supelco, PA, USA). The deposition targets (quartz round with diameter of 2") were positioned inside the quartz tube and the end was plugged with a small exhaust tube wrapped in ceramic wool to prevent O_2 from entering the chamber. The system was purged with preheated N_2 at a flow rate of 4.2 L/minute for 5 min prior to the start of run. Vegetable oil precursor was injected into the tube furnace at a rate of 5 mL/min for a total deposition time of 30 min. The tube furnace was then allowed to cool down under N_2 before the GUITAR coated substrates were removed.

Operando EC-AFM: The operando EC-AFM measurements were conducted using a Dimension Icon AFM (Bruker Nano, Santa Barbara, CA, U.S.A.) housed inside an argon-filled glovebox (M. Braun Inertgas-Systeme GmbH, Garching, Germany) with H_2O and O_2 concentrations below 0.1ppm. HOPG (SPI supplies, SPI-1 grade, 10x10x1mm, West Chester, PA, U.S.A.) and GUITAR samples were epoxied to one side etched PTFE disk (McMaster Carr, Elmhurst, IL, U.S.A.) and then mounted onto the electrochemical cell (Bruker Nano, Santa Barbara, CA, U.S.A.) as the working electrode. The exposed area of the electrode was approximately 1cm x 1cm. A fresh lithium strip (FMC Lithium) wrapped on a nickel wire (0.25mm dia, 99.98%, Alfa Aesar, Haverhill, MA, U.S.A.) was used as the counter electrode (length of ~5 cm) and reference electrode (length of ~0.5cm). The electrolyte used throughout this experiment was Gen II electrolyte (1.2M $LiPF_6$, in EC and EMC with weight ratio of 3:7 (w/w) supplied by our collaborators at Argonne National Lab and Idaho National Lab. Cyclic voltammetry (CV) was conducted by CH instrument 760E (Austin, TX, U.S.A.) with a potential range of 3V to 0.01V, starting from the open circuit potential (OCP) and scanning at 0.5 mV/s.

AFM images were obtained using silicon nitride ScanAsyst-Fluid probes (Bruker Nano) with a nominal tip radius of 20 nm and 0.7 N/m spring constant. Due to the relatively soft spring constant, the ScanAsyst-Fluid probes used here are best suited to measuring elastic moduli in the range of 1-20 MPa. Thus the modulus results here are only semi-quantitative and used to monitor the compositional evolution by providing a qualitative comparison of SEI hardness over time. To enable nanomechanical measurement of the electrode/SEI Young's modulus, the spring constant and deflection sensitivity of each probe was calibrated in the liquid electrolyte by the thermal tune method, while the tip radius (28 nm)

was measured with a Ti roughness standard (tip characterization sample, Bruker). To enable simultaneous measurement of sample topography and Young's modulus, AFM imaging was conducted in PeakForce QNM (Quantitative NanoMechanical) mode, with a scan rate of 0.5 Hz, sample rate of 256 samples/line, and a peak force of 2-5 nN. Raw AFM images were processed in Nano-Scope Analysis Version 2.0 (Bruker Nano, Santa Barbara, CA, USA) using a second order flatten to remove tilt and curvature. The SEI particle size can be estimated by using NanoScope Analysis's particle counting function.

Ex-situ XPS: XPS analysis was performed on PHI5600 Ultra X-ray photoelectron spectrometer using 1486.6 eV Al KαX-rays. To study the SEI formed at different potential ranges, linear scan voltammetry was applied to HOPG and GUITAR sample with a 3-electrode cell by scanning from the OCV to a desired potential (2V, 1.5V, 1V, 0.5V, and 0.01V) in Gen II electrolyte in an argon-filled glovebox. Samples were then rinsed with dimethyl carbonate (DMC) to remove residual salt and solvent and transferred to the XPS facility in a sealed transfer vessel to avoid exposure to air. The analyzed area of SEI was approximately 300 × 700 μm^2. Th pass energy for high resolution spectrum is 23.5 eV with 0.5 eV/step. The binding energies were referenced to the hydrocarbon C 1s photoelectron peak at 284.8 eV. Depth profiles were performed using 4 kV argon-ion sputtering, with ion current 0.13 μA. Sample charging, when present, was neutralized with a low-energy e-gun.

DFT calculations: Ethylene carbonate (EC) and lithium adsorption energies on the basal plane of graphene and graphite were calculated at the density functional theory (DFT) level with the Perdew−Burke−Ernzerhof (PBE) exchange-correlation functional[114] using the Vienna ab initio simulation package (VASP).[115-117] The interaction between the atomic cores and the electrons were described with the projector-augmented wave (PAW) method.[118, 119] Dispersion interactions

were described using the optimized optPBE-vdw[120] functional with a cutoff energy of 420 eV. The interlayer distance in graphite crystal with optPBE-vdw is predicted to be 3.34 Å, which agrees well with the experimental value of 3.35 Å.[121] The graphene calculations were performed using a 6 × 6 supercell and a 3× 3×1 Γ-centered Monkhorst-Pack k-point grid. Three graphene layers were selected to model the reactions on graphite[74-76] and the bottom layer was fixed during the calculations. In surface slab calculations, the ions are relaxed at a fixed cell shape and volume. Two common point defects were introduced into the graphene and graphite structures: the 5-7 members ring, known as Stone-Wales (SW) defect and single vacancy (SV) defect. Structure relaxations were performed until the residual force on each atom was less than 0.02 eV/Å and the total energy is converged within 10^{-4} eV. The adsorption energy (E_{ads}) at 0 K was calculated using equation (1) :

$$\Delta E_{ads} = E_{slab+adsorbate} - E_{slab} - E_{adsorbate} \quad (1)$$

where $E_{slab+adsorbate}$ and E_{slab} are the total electronic energies of the surface slab with and without the adsorbate; $E_{adsorbate}$ is the electronic energy of the adsorbate in gas phase, which was calculated with a 8.0 Å × 8.0 Å × 8.0 Å unit cell at the gamma point only.

Author Contributions

H. Xiong and H. Zhu conceived and designed all experiments. H. Zhu, P. Barnes, and C. Efaw conducted EChem-AFM experiments. H. Zhu, H. Xiong, E. Dufek, and P. Davis analyzed the EChem-AFM data. H. Zhu and J. Russell conducted XPS measurements and analysis. J. May, K. Hamal, and I.F. Cheng synthesized the GUITAR materials. H. Zhu, Z. Fang and L. Li conducted DFT calculations. H. Zhu, H. Xiong, J. Russell, E. Dufek, , Z. Fang, L. Lan, and P. Davis wrote the manuscript.

Acknowledgement

This work was supported by INL Laboratory Directed Research & Development (LDRD) Program under DOE Idaho Operations Office contract no. DE-AC07-05ID14517 with the

U.S. Department of Energy. Use of the environmental AFM was supported by NSF MRI [Grant No. 1727026]. XPS measurements were performed in the Boise State Atomic Films Laboratory. The authors are thankful to Dr. Chunrong Ma, Dr. Justin Connell, Dr. Elton Graugnard, and Dr. Steven Hues for fruitful discussion on the XPS data analysis. XPS measurements were performed in the Boise State Atomic Films Laboratory and the authors are grateful for the assistance of the measurements from members of the AFL. The authors would like to acknowledge the resources of the High-Performance Computing Center at Idaho National Laboratory, which is supported by the Office of Nuclear Energy of the U.S. Department of Energy and the Nuclear Science User Facilities under Contract No. DE-AC07-05ID14517 and also high-performance computing support of the R2 compute cluster (DOI: 10.18122/B2S41H) provided by Boise State University's Research Computing Department.

Conflict of interest

The authors declare no conflict of interest.

References

1. Armand, M.; Tarascon, J. M., *Nature* **2008,** *451* (7179), 652-657. DOI 10.1038/451652a.

2. Chu, S.; Majumdar, A., *Nature* **2012,** *488* (7411), 294-303. DOI 10.1038/nature11475.

3. Li, M.; Lu, J.; Chen, Z.; Amine, K., *Advanced Materials* **2018,** *30* (33), 1800561. DOI 10.1002/adma.201800561.

4. Blomgren, G. E., *Journal of The Electrochemical Society* **2016,** *164* (1), A5019-A5025. DOI 10.1149/2.0251701jes.

5. An, S. J.; Li, J.; Daniel, C.; Mohanty, D.; Nagpure, S.; Wood, D. L., *Carbon* **2016,** *105*, 52-76. DOI https://doi.org/10.1016/j.carbon.2016.04.008.

6. Verma, P.; Maire, P.; Novák, P., *Electrochimica Acta* **2010,** *55* (22), 6332-6341. DOI https://doi.org/10.1016/j.electacta.2010.05.072.

7. Peled, E.; Menkin, S., *Journal of The Electrochemical Society* **2017,** *164* (7), A1703-A1719. DOI 10.1149/2.1441707jes.

8. Peled, E., *Journal of The Electrochemical Society* **1979,** *126* (12), 2047-2051. DOI 10.1149/1.2128859.

9. Peled, E., *in Lithium Batteries*. New York, **1983**.

10. Peled, E.; Golodnitsky, D.; Ardel, G., *Journal of The Electrochemical Society* **1997,** *144* (8), L208-L210. DOI 10.1149/1.1837858.

11. Aurbach, D.; Markovsky, B.; Levi, M. D.; Levi, E.; Schechter, A.; Moshkovich, M.; Cohen, Y., *Journal of Power Sources* **1999,** *81-82*, 95-111. DOI https://doi.org/10.1016/S0378-7753(99)00187-1.

12. Christensen, J.; Newman, J., *Journal of The Electrochemical Society* **2004,** *151* (11), A1977. DOI 10.1149/1.1804812.

13. Edström, K.; Herstedt, M.; Abraham, D. P., *Journal of Power Sources* **2006,** *153* (2), 380-384. DOI https://doi.org/10.1016/j.jpowsour.2005.05.062.

14. Zhuang, G. V.; Xu, K.; Jow, T. R.; Ross, P. N., *Electrochemical and Solid-State Letters* **2004,** *7* (8), A224. DOI 10.1149/1.1756855.

15. Herstedt, M.; Abraham, D. P.; Kerr, J. B.; Edström, K., *Electrochimica Acta* **2004,** *49* (28), 5097-5110. DOI https://doi.org/10.1016/j.electacta.2004.06.021.

16. Cresce, A. v.; Russell, S. M.; Baker, D. R.; Gaskell, K. J.; Xu, K., *Nano Letters* **2014,** *14* (3), 1405-1412. DOI 10.1021/nl404471v.

17. Liu, T.; Lin, L.; Bi, X.; Tian, L.; Yang, K.; Liu, J.; Li, M.; Chen, Z.; Lu, J.; Amine, K.; Xu, K.; Pan, F., *Nature Nanotechnology* **2019,** *14* (1), 50-56. DOI 10.1038/s41565-018-0284-y.

18. Wang, L.; Menakath, A.; Han, F.; Wang, Y.; Zavalij, P. Y.; Gaskell, K. J.; Borodin, O.; Iuga, D.; Brown, S. P.; Wang, C.; Xu, K.; Eichhorn, B. W., *Nature Chemistry* **2019,** *11* (9), 789-796. DOI 10.1038/s41557-019-0304-z.

19. Tan, J.; Matz, J.; Dong, P.; Shen, J.; Ye, M., *Advanced Energy Materials* **2021,** *11* (16), 2100046. DOI https://doi.org/10.1002/aenm.202100046.

20. Yao, Y.-X.; Yan, C.; Zhang, Q., *Chemical Communications* **2020,** *56* (93), 14570-14584. DOI 10.1039/D0CC05084A.

21. Heiskanen, S. K.; Kim, J.; Lucht, B. L., *Joule* **2019,** *3* (10), 2322-2333. DOI https://doi.org/10.1016/j.joule.2019.08.018.

22. Zhang, Z.; Smith, K.; Jervis, R.; Shearing, P. R.; Miller, T. S.; Brett, D. J. L., *ACS Applied Materials & Interfaces* **2020,** *12* (31), 35132-35141. DOI 10.1021/acsami.0c11190.

23. Gajan, A.; Lecourt, C.; Torres Bautista, B. E.; Fillaud, L.; Demeaux, J.; Lucas, I. T., *ACS Energy Letters* **2021,** *6* (5), 1757-1763. DOI 10.1021/acsenergylett.1c00436.

24. Gauthier, M.; Carney, T. J.; Grimaud, A.; Giordano, L.; Pour, N.; Chang, H.-H.; Fenning, D. P.; Lux, S. F.; Paschos, O.; Bauer, C.; Maglia, F.; Lupart, S.; Lamp, P.; Shao-Horn, Y., *The Journal of Physical Chemistry Letters* **2015,** *6* (22), 4653-4672. DOI 10.1021/acs.jpclett.5b01727.

25. Xu, G.; Li, J.; Wang, C.; Du, X.; Lu, D.; Xie, B.; Wang, X.; Lu, C.; Liu, H.; Dong, S.; Cui, G.; Chen, L., *Angewandte Chemie International Edition* **2021,** *60* (14), 7770-7776. DOI https://doi.org/10.1002/anie.202013812.

26. Wang, A.; Kadam, S.; Li, H.; Shi, S.; Qi, Y., *npj Computational Materials* **2018,** *4* (1), 15. DOI 10.1038/s41524-018-0064-0.

27. Chattopadhyay, S.; Lipson, A. L.; Karmel, H. J.; Emery, J. D.; Fister, T. T.; Fenter, P. A.; Hersam, M. C.; Bedzyk, M. J., *Chemistry of Materials* **2012,** *24* (15), 3038-3043. DOI 10.1021/cm301584r.

28. Orsini, F.; Du Pasquier, A.; Beaudoin, B.; Tarascon, J. M.; Trentin, M.; Langenhuizen, N.; De Beer, E.; Notten, P., *Journal of Power Sources* **1998,** *76* (1), 19-29. DOI 10.1016/s0378-7753(98)00128-1.

29. Lei, J.; Li, L.; Kostecki, R.; Muller, R.; McLarnon, F., *Journal of The Electrochemical Society* **2005,** *152* (4), A774. DOI 10.1149/1.1867652.

30. Zeng, Z.; Liang, W. I.; Liao, H. G.; Xin, H. L.; Chu, Y. H.; Zheng, H., *Nano letters* **2014,** *14* (4), 1745-50. DOI 10.1021/nl403922u.

31. Steinhauer, M.; Stich, M.; Kurniawan, M.; Seidlhofer, B. K.; Trapp, M.; Bund, A.; Wagner, N.; Friedrich, K. A., *ACS applied materials & interfaces* **2017,** *9* (41), 35794-35801. DOI 10.1021/acsami.7b09181.

32. Domi, Y.; Ochida, M.; Tsubouchi, S.; Nakagawa, H.; Yamanaka, T.; Doi, T.; Abe, T.; Ogumi, Z., *The Journal of Physical Chemistry C* **2011,** *115* (51), 25484-25489. DOI 10.1021/jp2064672.

33. Chu, A. C.; Josefowicz, J. Y.; Farrington, G. C., *Journal of The Electrochemical Society* **1997,** *144* (12), 4161-4169. DOI 10.1149/1.1838160.

34. Hirasawa, K. A.; Sato, T.; Asahina, H.; Yamaguchi, S.; Mori, S., *Journal of The Electrochemical Society* **1997,** *144* (4), L81-L84. DOI 10.1149/1.1837560.

35. Jeong, S.-K.; Inaba, M.; Mogi, R.; Iriyama, Y.; Abe, T.; Ogumi, Z., *Langmuir* **2001,** *17* (26), 8281-8286. DOI 10.1021/la015553h.

36. Jeong, S.-K.; Inaba, M.; Abe, T.; Ogumi, Z., *Journal of The Electrochemical Society* **2001,** *148* (9), A989. DOI 10.1149/1.1387981.

37. Shen, C.; Wang, S.; Jin, Y.; Han, W. Q., *ACS Appl Mater Interfaces* **2015,** *7* (45), 25441-7. DOI 10.1021/acsami.5b08238.

38. Inaba, M.; Siroma, Z.; Kawatate, Y.; Funabiki, A.; Ogumi, Z., *Journal of Power Sources* **1997,** *68* (2), 221-226. DOI https://doi.org/10.1016/S0378-7753(96)02555-4.

39. Luchkin, S. Y.; Lipovskikh, S. A.; Katorova, N. S.; Savina, A. A.; Abakumov, A. M.; Stevenson, K. J., *Scientific reports* **2020,** *10* (1), 8550. DOI 10.1038/s41598-020-65552-6.

40. Weber, I.; Schnaidt, J.; Wang, B.; Diemant, T.; Behm, R. J., *ChemElectroChem* **2019,** *6* (19), 4985-4997. DOI 10.1002/celc.201900909.

41. Peled, E.; Golodnitsky, D.; Ulus, A.; Yufit, V., *Electrochimica Acta* **2004,** *50* (2), 391-395. DOI https://doi.org/10.1016/j.electacta.2004.01.130.

42. Peled, E.; Tow, D. B.; Merson, A.; Gladkich, A.; Burstein, L.; Golodnitsky, D., *Journal of Power Sources* **2001,** *97-8*, 52-57. DOI Doi 10.1016/S0378-7753(01)00505-5.

43. Tsubouchi, S.; Domi, Y.; Doi, T.; Ochida, M.; Nakagawa, H.; Yamanaka, T.; Abe, T.; Ogumi, Z., *Journal of The Electrochemical Society* **2012,** *159* (11), A1786-A1790. DOI 10.1149/2.028211jes.

44. Yoshio, M.; Wang, H.; Fukuda, K.; Hara, Y.; Adachi, Y., *Journal of The Electrochemical Society* **2000,** *147* (4), 1245. DOI 10.1149/1.1393344.

45. Yoshio, M.; Wang, H.; Fukuda, K., *Angewandte Chemie (International ed. in English)* **2003,** *42* (35), 4203-6. DOI 10.1002/anie.200351203.

46. Rohman, F.; Azizah, U.; Prihandoko, B., *AIP Conference Proceedings* **2017,** *1823* (1), 020040. DOI 10.1063/1.4978113.

47. Amiruddin, S.; Joachin, H.; Li, B.; Prakash, J., *ECS Transactions* **2019,** *6* (25), 191-197. DOI 10.1149/1.2943238.

48. Kabir, H.; Zhu, H.; May, J.; Hamal, K.; Kan, Y.; Williams, T.; Echeverria, E.; McIlroy, D. N.; Estrada, D.; Davis, P. H.; Pandhi, T.; Yocham, K.; Higginbotham, K.; Clearfield, A.; Cheng, I. F., *Carbon* **2019,** *144*, 831-840. DOI https://doi.org/10.1016/j.carbon.2018.12.058.

49. Kabir, H.; Zhu, H.; May, J.; Hamal, K.; Kan, Y.; Williams, T.; Echeverria, E.; McIlroy, D. N.; Estrada, D.; Davis, P. H.; Pandhi, T.; Yocham, K.; Higginbotham, K.; Clearfield, A.; Cheng, I. F., *Carbon* **2018,** *144*, 831-840. DOI 10.1016/j.carbon.2018.12.058.

50. Gyan, I. O.; Wojcik, P. M.; Aston, D. E.; McIlroy, D. N.; Cheng, I. F., *ChemElectroChem* **2015,** *2* (5), 700-706. DOI https://doi.org/10.1002/celc.201402433.

51. Zhou, L.-J.; Hou, Z. F.; Wu, L.-M., *The Journal of Physical Chemistry C* **2012,** *116* (41), 21780-21787. DOI 10.1021/jp304861d.

52. Fan, X.; Zheng, W. T.; Kuo, J.-L., *ACS Applied Materials & Interfaces* **2012,** *4* (5), 2432-2438. DOI 10.1021/am3000962.

53. Okamoto, Y., *The Journal of Physical Chemistry C* **2016,** *120* (26), 14009-14014. DOI 10.1021/acs.jpcc.6b05458.

54. Wang, Y.; Nakamura, S.; Ue, M.; Balbuena, P. B., *Journal of the American Chemical Society* **2001,** *123* (47), 11708-11718. DOI 10.1021/ja0164529.

55. Bozorgchenani, M.; Buchner, F.; Forster-Tonigold, K.; Kim, J.; Groß, A.; Behm, R. J., *Langmuir* **2018,** *34* (29), 8451-8463. DOI 10.1021/acs.langmuir.8b01054.

56. Wang, Y.; Alsmeyer, D. C.; McCreery, R. L., *Chemistry of Materials* **1990,** *2* (5), 557-563. DOI 10.1021/cm00011a018.

57. Ferrari, A. C., *Solid State Communications* **2007,** *143* (1), 47-57. DOI https://doi.org/10.1016/j.ssc.2007.03.052.

58. Ferrari, A. C.; Robertson, J.; Ferrari, A. C.; Robertson, J., *Philosophical Transactions of the Royal Society of London. Series A: Mathematical, Physical and Engineering Sciences* **2004,** *362* (1824), 2477-2512. DOI doi:10.1098/rsta.2004.1452.

59. Ferrari, A. C., *Diamond and Related Materials* **2002,** *11* (3), 1053-1061. DOI https://doi.org/10.1016/S0925-9635(01)00730-0.

60. Ferrari, A. C.; Robertson, J., *Physical Review B* **2000,** *61* (20), 14095-14107. DOI 10.1103/PhysRevB.61.14095.

61. Campana, F. P.; Kötz, R.; Vetter, J.; Novák, P.; Siegenthaler, H., *Electrochemistry Communications* **2005,** *7* (1), 107-112. DOI https://doi.org/10.1016/j.elecom.2004.11.015.

62. Novák, P.; Joho, F.; Imhof, R.; Panitz, J.-C.; Haas, O., *Journal of Power Sources* **1999,** *81-82*, 212-216. DOI https://doi.org/10.1016/S0378-7753(99)00119-6.

63. Andersson, A. M.; Edström, K., *Journal of The Electrochemical Society* **2001,** *148* (10), A1100. DOI 10.1149/1.1397771.

64. Shen, C.; Wang, S.; Jin, Y.; Han, W.-Q., *ACS Applied Materials & Interfaces* **2015,** *7* (45), 25441-25447. DOI 10.1021/acsami.5b08238.

65. Yuan, W.; Zhou, Y.; Li, Y.; Li, C.; Peng, H.; Zhang, J.; Liu, Z.; Dai, L.; Shi, G., *Scientific Reports* **2013,** *3* (1), 2248. DOI 10.1038/srep02248.

66. Velický, M.; Toth, P. S.; Woods, C. R.; Novoselov, K. S.; Dryfe, R. A. W., *The Journal of Physical Chemistry C* **2019,** *123* (18), 11677-11685. DOI 10.1021/acs.jpcc.9b01010.

67. Shen, C.; Hu, G.; Cheong, L.-Z.; Huang, S.; Zhang, J.-G.; Wang, D., *Small Methods* **2018,** *2* (2), 1700298. DOI https://doi.org/10.1002/smtd.201700298.

68. Xu, K.; Lam, Y.; Zhang, S. S.; Jow, T. R.; Curtis, T. B., *The Journal of Physical Chemistry C* **2007,** *111* (20), 7411-7421. DOI 10.1021/jp068691u.

69. Xu, K.; Zhuang, G. V.; Allen, J. L.; Lee, U.; Zhang, S. S.; Ross, P. N.; Jow, T. R., *The Journal of Physical Chemistry B* **2006,** *110* (15), 7708-7719. DOI 10.1021/jp0601522.

70. Mochida, I.; Ku, C.-H.; Korai, Y., *Carbon* **2001,** *39* (3), 399-410. DOI https://doi.org/10.1016/S0008-6223(00)00137-8.

71. Jow, T. R.; Xu, K.; Borodin, O.; Ue, M., *Electrolytes for Lithium and Lithium-Ion Batteries*. Springer: New York, NY, **2014**.

72. Bronsted, J. N., *Chemical Reviews* **1928,** *5* (3), 231-338. DOI 10.1021/cr60019a001.

73. Evans, M. G.; Polanyi, M., *Transactions of the Faraday Society* **1938,** *34* (0), 11-24. DOI 10.1039/TF9383400011.

74. Fang, Z.; Li, L.; Dixon, D. A.; Fushimi, R. R.; Dufek, E. J., *The Journal of Physical Chemistry C* **2021,** *125* (37), 20686-20696. DOI 10.1021/acs.jpcc.1c06741.

75. Klintenberg, M.; Lebègue, S.; Ortiz, C.; Sanyal, B.; Fransson, J.; Eriksson, O., *Journal of Physics: Condensed Matter* **2009,** *21* (33), 335502. DOI 10.1088/0953-8984/21/33/335502.

76. Valencia, F.; Romero, A. H.; Ancilotto, F.; Silvestrelli, P. L., *The Journal of Physical Chemistry B* **2006,** *110* (30), 14832-14841. DOI 10.1021/jp062126+.

77. Howard, J. D.; Assary, R. S.; Curtiss, L. A., *The Journal of Physical Chemistry C* **2020,** *124* (5), 2799-2805. DOI 10.1021/acs.jpcc.9b10403.

78. Li, T.; Xing, L.; Li, W.; Wang, Y.; Xu, M.; Gu, F.; Hu, S., *Journal of Power Sources* **2013,** *244*, 668-674. DOI https://doi.org/10.1016/j.jpowsour.2012.12.062.

79. Xie, W.; Weng, L.-T.; Ng, K. M.; Chan, C. K.; Chan, C.-M., *Carbon* **2017,** *112*, 192-200. DOI https://doi.org/10.1016/j.carbon.2016.11.002.

80. Fingerle, M.; Späth, T.; Schulz, N.; Hausbrand, R., *Chemical Physics* **2017,** *498-499*, 19-24. DOI https://doi.org/10.1016/j.chemphys.2017.09.004.

81. Buchner, F.; Farkhondeh, H.; Bozorgchenani, M.; Uhl, B.; Behm, R. J., *Physical Chemistry Chemical Physics* **2014,** *16* (23), 11191-11195. DOI 10.1039/C4CP01417K.

82. Bozorgchenani, M.; Naderian, M.; Farkhondeh, H.; Schnaidt, J.; Uhl, B.; Bansmann, J.; Groß, A.; Behm, R. J.; Buchner, F., *The Journal of Physical Chemistry C* **2016,** *120* (30), 16791-16803. DOI 10.1021/acs.jpcc.6b05012.

83. Aurbach, D., *Journal of Power Sources* **2003,** *119-121*, 497-503. DOI https://doi.org/10.1016/S0378-7753(03)00273-8.

84. Kang, S. H.; Abraham, D. P.; Xiao, A.; Lucht, B. L., *Journal of Power Sources* **2008,** *175* (1), 526-532. DOI https://doi.org/10.1016/j.jpowsour.2007.08.112.

85. Xu, M.; Li, W.; Lucht, B. L., *Journal of Power Sources* **2009,** *193* (2), 804-809. DOI https://doi.org/10.1016/j.jpowsour.2009.03.067.

86. Vogdanis, L.; Heitz, W., *Die Makromolekulare Chemie, Rapid Communications* **1986,** *7* (9), 543-547. DOI https://doi.org/10.1002/marc.1986.030070901.

87. Peled, E.; Towa, D. B.; Merson, A.; Burstein, L., *Journal of New Materials for Electrochemical Systems* **2000,** *3* (4), 321-328.

88. Xu, C.; Sun, B.; Gustafsson, T.; Edström, K.; Brandell, D.; Hahlin, M., *Journal of Materials Chemistry A* **2014,** *2* (20), 7256-7264. DOI 10.1039/C4TA00214H.

89. Ma, Y.; Zhou, Y.; Du, C.; Zuo, P.; Cheng, X.; Han, L.; Nordlund, D.; Gao, Y.; Yin, G.; Xin, H. L.; Doeff, M. M.; Lin, F.; Chen, G., *Chemistry of Materials* **2017,** *29* (5), 2141-2149. DOI 10.1021/acs.chemmater.6b04784.

90. Tatara, R.; Karayaylali, P.; Yu, Y.; Zhang, Y.; Giordano, L.; Maglia, F.; Jung, R.; Schmidt, J. P.; Lund, I.; Shao-Horn, Y., *Journal of The Electrochemical Society* **2018,** *166* (3), A5090-A5098. DOI 10.1149/2.0121903jes.

91. Peled, E.; Golodnitsky, D.; Menachem, C.; Bar-Tow, D., *Journal of The Electrochemical Society* **1998,** *145* (10), 3482-3486. DOI 10.1149/1.1838831.

92. Peled, E.; Bar Tow, D.; Merson, A.; Gladkich, A.; Burstein, L.; Golodnitsky, D., *Journal of Power Sources* **2001,** *97-98*, 52-57. DOI https://doi.org/10.1016/S0378-7753(01)00505-5.

93. Aurbach, D.; Markovsky, B.; Shechter, A.; Ein-Eli, Y.; Cohen, H., *Journal of The Electrochemical Society* **1996,** *143* (12), 3809-3820. DOI 10.1149/1.1837300.

94. He, M.; Guo, R.; Hobold, G. M.; Gao, H.; Gallant, B. M., *Proceedings of the National Academy of Sciences* **2020,** *117* (1), 73-79. DOI 10.1073/pnas.1911017116.

95. Cui, C.; Yang, C.; Eidson, N.; Chen, J.; Han, F.; Chen, L.; Luo, C.; Wang, P.-F.; Fan, X.; Wang, C., *Advanced Materials* **2020,** *32* (12), 1906427. DOI https://doi.org/10.1002/adma.201906427.

96. Zhang, L.; Zhang, K.; Shi, Z.; Zhang, S., *Langmuir* **2017,** *33* (42), 11164-11169. DOI 10.1021/acs.langmuir.7b02031.

97. Kim, K. H.; Cho, J. H.; Hwang, J. U.; Im, J. S.; Lee, Y.-S., *Journal of Industrial and Engineering Chemistry* **2021,** *99*, 48-54. DOI https://doi.org/10.1016/j.jiec.2021.04.002.

98. Eshkenazi, V.; Peled, E.; Burstein, L.; Golodnitsky, D., *Solid State Ionics* **2004,** *170* (1), 83-91. DOI https://doi.org/10.1016/S0167-2738(03)00107-3.

99. Xu, K.; Lee, U.; Zhang, S. S.; Jow, T. R., *Journal of The Electrochemical Society* **2004,** *151* (12), A2106. DOI 10.1149/1.1812732.

100. Xu, K., *Chemical Reviews* **2004,** *104* (10), 4303-4418. DOI 10.1021/cr030203g.

101. Kawamura, T.; Kimura, A.; Egashira, M.; Okada, S.; Yamaki, J.-I., *Journal of Power Sources* **2002,** *104* (2), 260-264. DOI https://doi.org/10.1016/S0378-7753(01)00960-0.

102. Sloop, S. E.; Pugh, J. K.; Wang, S.; Kerr, J. B.; Kinoshita, K., *Electrochemical and Solid-State Letters* **2001,** *4* (4), A42. DOI 10.1149/1.1353158.

103. Aurbach, D.; Levi, M. D.; Levi, E.; Schechter, A., *The Journal of Physical Chemistry B* **1997,** *101* (12), 2195-2206. DOI 10.1021/jp962815t.

104. Aurbach, D.; Markovsky, B.; Weissman, I.; Levi, E.; Ein-Eli, Y., *Electrochimica Acta* **1999,** *45* (1), 67-86. DOI https://doi.org/10.1016/S0013-4686(99)00194-2.

105. Aurbach, D., *Journal of Power Sources* **2000,** *89* (2), 206-218. DOI https://doi.org/10.1016/S0378-7753(00)00431-6.

106. Balbuena, P. B.; Wang, Y.; Dawsonera, *Lithium-ion batteries solid-electrolyte interphase*. Imperial College Press: London, **2004**.

107. Li, Y.; Xu, B.; Xu, H.; Duan, H.; Lü, X.; Xin, S.; Zhou, W.; Xue, L.; Fu, G.; Manthiram, A.; Goodenough, J. B., *Angewandte Chemie International Edition* **2017,** *56* (3), 753-756. DOI https://doi.org/10.1002/anie.201608924.

108. Yildirim, H.; Kinaci, A.; Chan, M. K. Y.; Greeley, J. P., *ACS Applied Materials & Interfaces* **2015,** *7* (34), 18985-18996. DOI 10.1021/acsami.5b02904.

109. Pan, J.; Cheng, Y.-T.; Qi, Y., *Physical Review B* **2015,** *91* (13), 134116. DOI 10.1103/PhysRevB.91.134116.

110. Monroe, C.; Newman, J., *Journal of The Electrochemical Society* **2004,** *151* (6), A880. DOI 10.1149/1.1710893.

111. Shiraishi, S.; Kanamura, K.; Takehara, Z.-i., *Langmuir* **1997,** *13* (13), 3542-3549. DOI 10.1021/la960876c.

112. Shiraishi, S.; Kanamura, K.; Takehara, Z. i., *Journal of The Electrochemical Society* **1999,** *146* (5), 1633-1639. DOI 10.1149/1.1391818.

113. Klein, S.; van Wickeren, S.; Röser, S.; Bärmann, P.; Borzutzki, K.; Heidrich, B.; Börner, M.; Winter, M.; Placke, T.; Kasnatscheew, J., *Advanced Energy Materials* **2021,** *11* (14), 2003738. DOI https://doi.org/10.1002/aenm.202003738.

114. Perdew, J. P.; Burke, K.; Ernzerhof, M., *Physical Review Letters* **1996,** *77* (18), 3865-3868. DOI 10.1103/PhysRevLett.77.3865.

115. Kresse, G.; Furthmüller, J., *Computational Materials Science* **1996,** *6* (1), 15-50. DOI https://doi.org/10.1016/0927-0256(96)00008-0.

116. Kresse, G.; Hafner, J., *Physical Review B* **1993,** *48* (17), 13115-13118. DOI 10.1103/PhysRevB.48.13115.

117. Kresse, G.; Hafner, J., *Physical Review B* **1993,** *47* (1), 558-561. DOI 10.1103/PhysRevB.47.558.

118. Kresse, G.; Joubert, D., *Physical Review B* **1999,** *59* (3), 1758-1775. DOI 10.1103/PhysRevB.59.1758.

119. Blöchl, P. E., *Physical Review B* **1994,** *50* (24), 17953-17979. DOI 10.1103/PhysRevB.50.17953.

120. Klimeš, J.; Bowler, D. R.; Michaelides, A., *Journal of Physics: Condensed Matter* **2009,** *22* (2), 022201. DOI 10.1088/0953-8984/22/2/022201.

121. Harrison, W. A., *Electronic Structure and the Properties of Solids: the Physics of the Chemical Bond.* . W. H. Freeman and Company,: San Francisco, **1980**.